UVicSPACE: Research & Learning Repository

University of Victoria

Faculty of Science

Faculty Publications

This is a post-print version of the following article:

Microfluidic Shear Processing Control of Biological Reduction Stimuli-Responsive Polymer Nanoparticles for Drug Delivery

Yuhang Huang, Arman Moini Jazani, Elliot P. Howell, Lisa A. Reynolds, Jung Kwon Oh, & Matthew G. Moffitt

July 2020

The final publication is available at:

https://doi.org/10.1021/acsbiomaterials.0c00896

Citation for this paper:

Huang, Y., Jazani, A. M., Howell, E. P., Reynolds, L. A., Oh, J. K., & Moffitt, M. G. (2020). Microfluidic Shear Processing Control of Biological Reduction Stimuli-Responsive Polymer Nanoparticles for Drug Delivery. *ACS Biomaterials Science & Engineering*, 6(9), 5069-5083. https://doi.org/10.1021/acsbiomaterials.0c00896.

Microfluidic Shear Processing Control of Biological Reduction Stimuli-Responsive Polymer Nanoparticles for Drug Delivery

Yuhang Huang, Arman Moini Jazani,[¥] Elliot P. Howell, Lisa A. Reynolds,[†] Jung Kwon Oh,[¥] and Matthew G. Moffitt*

Department of Chemistry, University of Victoria, PO Box 1700 Stn CSC, Victoria, BC V8W 2Y2, Canada

[¥]*Department of Chemistry and Biochemistry, Concordia University, 7141 Sherbrooke St. West, Montreal, Quebec H4B 1R6, Canada*

[†]*Department of Biochemistry and Microbiology, University of Victoria, PO Box 1700 Stn CSC, Victoria, BC V8W 2Y2, Canada*

Abstract

We demonstrate microfluidic manufacturing of glutathione (GSH)-responsive polymer nanoparticles (PNPs) with controlled *in vitro* pharmacological properties for selective drug delivery. This work leverages previous fundamental work on microfluidic control of the physicochemical properties of GSH-responsive PNPs containing cleavable disulfide groups in two different locations (core and interface, DualM PNPs). In this paper, we employ a two-phase gas-liquid microfluidic reactor for the flow-directed manufacturing of paclitaxel-loaded or DiI-loaded DualM PNPs (PAX-PNPs or DiI-PNPs, where DiI is a fluorescent drug surrogate dye). We find both PAX-PNPs and DiI-PNPs exhibit similar flow-tunable sizes, morphologies, and internal structures to those previously described for empty DualM PNPs. Fluorescent imaging of DiI-PNP formulations shows that microfluidic manufacturing greatly improves the homogeneity of drug dispersion within the PNP population compared to standard bulk microprecipitation. Encapsulation of PAX in DualM PNPs significantly increases its selectivity to cancerous cells, with various PAX-PNP formulations showing higher cytotoxicity against cancerous MCF-7 cells than against non-cancerous HaCaT cells, in contrast to free PAX which showed similar cytotoxicity in the two cell lines. In addition, characterization of DualM PNP formulations formed at various

Email: mmoffitt@uvic.ca

microfluidic flow rates reveals that critical figures of merit for drug delivery function—including encapsulation efficiencies, GSH-triggered release rates, rates of cell uptake, cytotoxicities, and selectivity to cancerous cells— exhibit microfluidic flow tunability that mirror trends in PNP size. These results highlight the potential of two-phase microfluidic manufacturing to controlling both structure and drug delivery function of biological stimuli-responsive nanomedicines toward improved therapeutic outcomes.

Keywords: reduction-responsive block copolymers, microfluidics, directed self-assembly, nanoparticles, drug delivery

Introduction

Polymer nanoparticles (PNPs) formed from self-assembly of amphiphilic block copolymers in aqueous media are promising candidates for drug delivery.[1-12] The hydrophobic cores of PNPs encapsulate hydrophobic drugs while the surrounding hydrophilic coronae enable dispersion in the blood, increasing drug bioavailability.[2, 6, 13-14] Encapsulation in PNPs has also been shown to decrease the side effects of relatively indiscriminate anticancer agents by increasing tumor localization.[13, 15-17] Furthermore, the sizes and morphologies of PNPs, which are critical factors influencing nanoparticle transport and cell uptake, can be controlled *via* the self-assembly conditions.[18-21]

The cellular reducing agent glutathione (GSH) is overexpressed in cancer cells,[22-23] providing a strategy for increased selectivity *via* GSH-triggered degradation of stimuli-responsive block copolymers and concomitant drug release from the PNPs at the tumor site (Figure 1A). For example, in the presence of GSH, disulfide linkages

introduced into block copolymers will be cleaved to the corresponding thiols.[24-30] We have previously demonstrated the synthesis of GSH-responsive block copolymers with disulfide linkages in both junction and pendant locations.[31] Self-assembly of the resulting block copolymers in aqueous media form "DualM" PNPs consisting of hydrophilic poly(ethylene oxide) (PEO) coronal chains and hydrophobic polymethacrylate cores (Figure 1B). The core-forming blocks possess disulfide pendants (PHMssEt) with disulfide junctions between the hydrophobic and hydrophilic blocks (PEO-ss-PHMssEt). The DualM PNPs showed evidence of synergistically-enhanced drug release inside HeLa cells supplemented with 10 mM GSH enabled by the dual locations of cleavable disulfide linkages.[31]

Conventional bottom-up manufacturing of PNPs relies on changes in the chemistry of the formulation, including the block copolymer composition, initial solvent, and drug-to-polymer ratio, for tuning the structure and drug delivery properties of the resulting PNPs.[32-35] Microfluidic approaches to PNP manufacturing provide opportunities for increased control over the drug delivery functionality of nanomedicines.[36-39] Further, microfluidics shows promising potential for scaling-up PNP manufacturing since parallel production and fast screening of formulation conditions can be achieved.[34] Our group has employed a two-phase gas-liquid segmented microfluidic reactor (Figure 2) for PNP manufacturing from various block copolymer materials, demonstrating that variable flow rate provides a convenient experimental handle on top-down processing control over PNP structure and

properties.[40-55] Microfluidic PNP control in these reactors is attributed to a combination of particle coalescence, particle break-up, and intraparticle chain rearrangements enabled by flow-variable processing in high-shear "hot spots" within the microchannels.[40-43, 46] This is in contrast to more common single-phase microfluidic reactors for PNP manufacturing, including a commercial staggered herringbone microfluidic mixer, which provide fast mixing but without the structural control enabled by high-shear processing.[47]

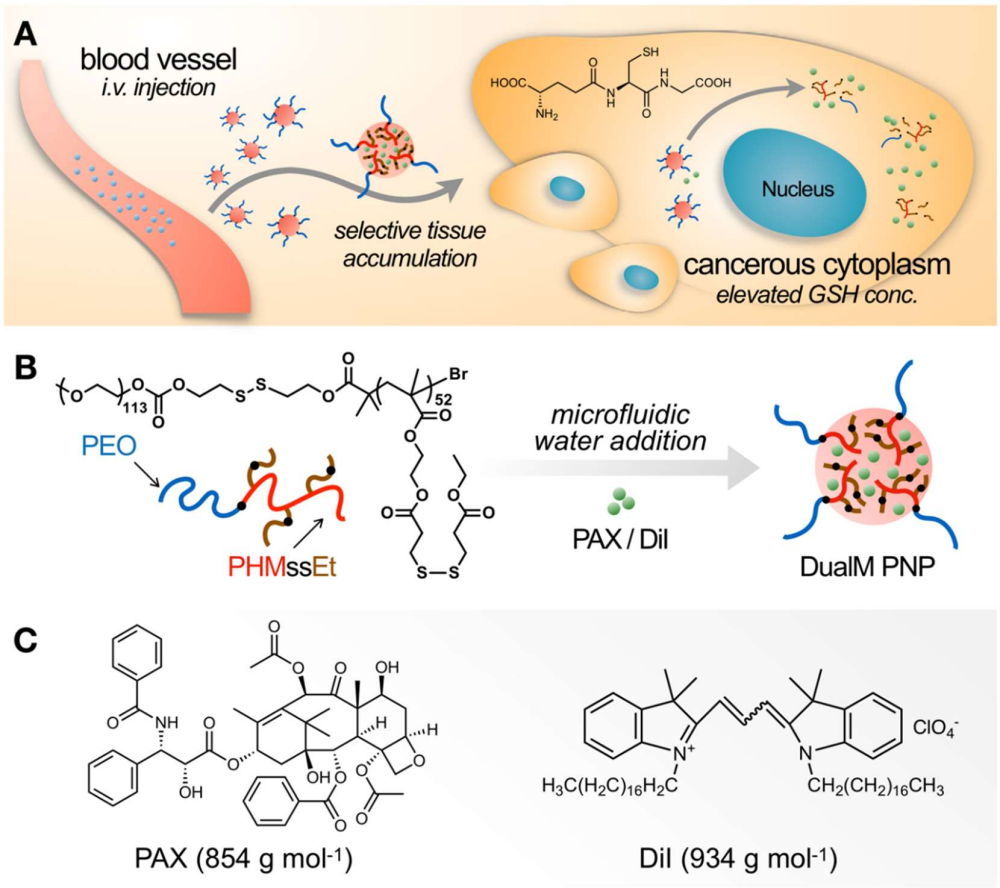

Figure 1. Schematics of (A) the hypothesized targeting and controlled release of drug encapsulated in DualM PNPs; (B) the molecular structure and aqueous self-assembly

of PEO-ss-PHMssEt block copolymers and the general structure of the resulting DualM PNPs. (C) Molecular structures of PAX and DiI.

More recently, we used a two-phase microfluidic reactor to produce DualM PNPs (Figure 1B) with sizes, morphologies, and internal structures that were tunable with manufacturing flow rate.[55] This initial study focused on a fundamental understanding of on-chip DualM PNP manufacturing, including a self-assembly mechanism based on the interplay of PNP thermodynamics and shear-activated formation pathways. We also showed that GSH responsivities of the PNPs depended strongly on their flow-controlled size and structure. Specifically, PNPs with smaller mean sizes showed faster GSH-triggered size increase, attributed to junction cleavage, and PNPs with higher excess Gibbs free energy showed faster inner compartment growth, attributed to pendant cleavage. We concluded that the combination of chemical control of functional group location and microfluidic processing control of PNP size and structure enables increased tunability of biological responsivities, with promising implications for drug delivery applications. However, no hydrophobic drugs or drug surrogates were encapsulated within the DualM PNPs in that initial study, such that microfluidic control of drug delivery properties could not be determined.

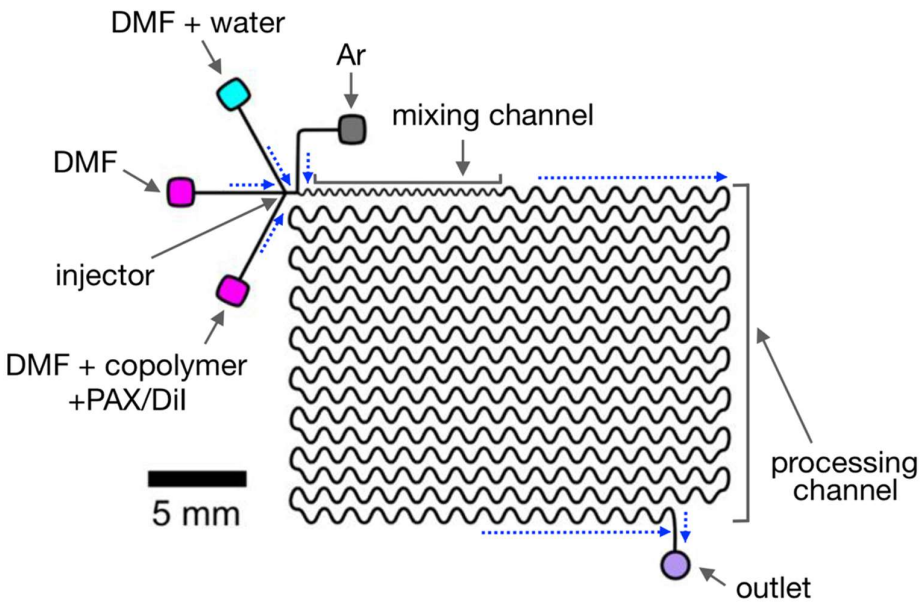

Figure 2. Schematic of two-phase gas-liquid microfluidic reactor.

In this paper, we extend our previous fundamental insights into microfluidic control of nanoparticle structure,[55] in order to establish manufacturing flow-tunability of the pharmacological properties of biologically responsive PNPs. Through a process chain of microfluidic formulation, physical characterization, and biological assessment, we develop powerful manufacturing-structure-property relationships that provide a pathway to optimization of selective nanomedicines through engineering. Specifically, we apply flow-controlled microfluidic manufacturing to produce DualM GSH-responsive PNPs (Figure 1B) containing either the anticancer drug paclitaxel (PAX) or the fluorescent drug surrogate dye 1,1′-dioctadecyl-3,3,3′,3′-tetramethylindocarbocyanine perchlorate (DiI). By encapsulating two hydrophobic molecules with similar molecular weights but different molecular structures (Figure 1C) and miscibilities with PHMssEt cores, we obtain important insights into the effect of

the drug molecules on the sizes and morphologies of different nanomedicines prepared under the same microfluidic conditions. In addition, the anticancer properties of PAX-PNPs and the fluorescent properties of DiI-PNPs provide opportunities for probing different drug delivery properties of flow-directed DualM PNPs. Similar to DualM PNPs without PAX, we demonstrate microfluidic flow control over initial sizes, morphologies, internal structures, and GSH responsivities. More importantly, we show that microfluidic flow rate provides a unique control handle over various DualM PNP drug delivery characteristics, including encapsulation efficiencies and homogeneities, GSH-triggered release kinetics, cell uptake, and GSH-dependent *in vitro* cytotoxicities.

Results and Discussion

Effect of Flow Rate on Mean Hydrodynamic Sizes and Polydispersities of PAX-Loaded and DiI-Loaded DualM PNPs. Dynamic light scattering experiments were carried out for all PNP formulations, with cumulant analysis yielding hydrodynamic size and polydispersity information (Figure 3). Figure 3A shows mean hydrodynamic effective diameters ($d_{h,eff}$) of DualM PNPs at various flow rates (Q = 0, 50, 100, and 200 μL/min), where Q = 0 μL/min indicates PNPs prepared by the bulk nanoprecipitation method. For each manufacturing condition, data is shown for three cases of hydrophobic molecule encapsulation: 1. PNPs with no encapsulated molecules ("empty" PNPs, white bars); 2. PNPs with encapsulated PAX (PAX-PNPs, blue bars);

and 3. PNPs with encapsulated DiI (DiI-PNPs, red bars). The indicated sizes for empty PNPs were previously reported in our recent study (ref. 55) and are shown here for comparison purposes.

Although PAX and DiI molecules have similar molecular weights (854 and 934 g mol^{-1}, respectively), the two long alkyl hydrocarbon tails impart DiI with greater free volume than PAX (Figure 1C), such that encapsulated DiI would be expected to swell the hydrophobic domains more extensively than PAX. However, for each flow condition we find that the three encapsulation cases (empty, PAX and DiI) show statistically identical $d_{h,eff}$ values (Figure 3A), suggesting that the overall PNP sizes are not affected by the addition of either hydrophobic molecule to the PNPs. This interesting result suggests either that the hydrophobic domains are not significantly swollen by either PAX or DiI, or that changes in the internal PNP structure compensate for swelling differences to maintain consistent PNP sizes. This question will be addressed in the next section with TEM data showing the internal structure of DualM PNPs containing different encapsulated molecules.

Due to the size similarities of empty PNPs, PAX-PNPs and DiI-PNPs for each flow condition, all three cases show the same trend with respect to flow rate (Figure 3A). This trend was previously explained by the competition between shear-induced particle coalescence and shear-induced particle breakup as the maximum shear rate in the hot spots increased with increasing flow rate.[55] Briefly, shear-induced coalescence events in the microchannels effect increases in mean hydrodynamic sizes between Q =

0 μL/min and Q = 50 μL/min. Next, particle growth in the microchannels increases particle capillary numbers, increasing the role of shear-induce particle breakup such that mean hydrodynamic sizes drop between Q = 50 μL/min and Q = 100 μL/min. Finally, as the maximum shear rate is further increased, the competition between coalescence and breakup events leads to small increases in mean hydrodynamic sizes between Q = 100 μL/min and Q = 200 μL/min.

Similar to mean hydrodynamic sizes, the polydispersities of PAX-PNPs and DiI-PNPs show a similar trend with increasing flow rate to that of empty DualM PNPs (Figure 3B). Polydispersity values for the empty DualM PNPs reported in our previous study are shown for comparison.[55] Specifically, polydispersities for all three encapsulation cases are found to drop significantly between Q = 0 μL/min and Q = 50 μL/min, with no significant changes in polydispersities found at higher microfluidic flow rates. As described previously,[55] this trend is explained by shear-induced coalescence of small particles in the microchannels decreasing the distribution width compared to bulk-formed PNPs, while the competition between shear-induced coalescence and shear-induced breakup leads to similar polydispersities as the flow rate is further increased.

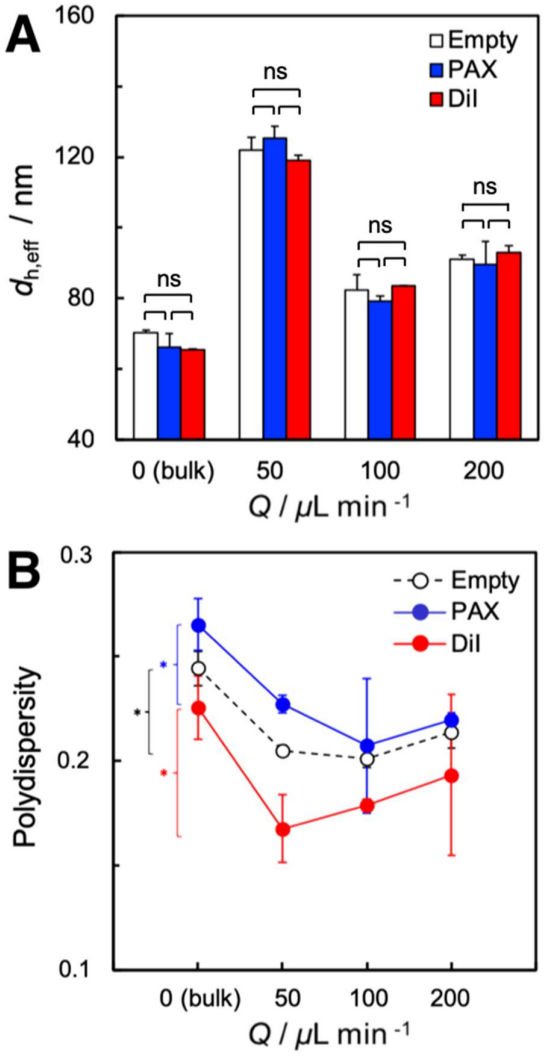

Figure 3. Hydrodynamic effective diameters ($d_{h,eff}$, A) and polydispersities (B) of empty PNPs (white), PAX-PNPs (blue), and DiI-PNPs (red) manufactured at various flow rates (Q = 50, 100, and 200 μL/min) using the microfluidic reactor or bulk nanoprecipitation (Q = 0 μL/min). Brackets indicate statistical comparisons between $d_{h,eff}$ and polydispersities of PNPs manufactured under different conditions: * indicates $p < 0.05$ and ns indicates $p > 0.05$.

Effect of Flow Rate on Morphologies of PAX-Loaded and DiI-Loaded DualM

PNPs. Flow-tunable shear forces were previously shown to have a strong effect on the

morphologies and internal structures of DualM PNPs prepared in the two-phase microfluidic reactor, due to the shear rate-dependent interplay of particle coalescence, particle breakup, and intraparticle chain rearrangements.[55] Remarkably, we find that encapsulating either PAX or DiI using the same DualM copolymer results in nearly identical mixtures of morphologies as the empty PNPs at the same investigated flow condition (Figure 4 and Table 1). The representative TEM images in Figure 4 were obtained following uranyl acetate staining, such that the hydrophilic PEO regions appear dark while the hydrophobic PHMssEt regions appear bright. Table 1 lists mean core dimensions and number percentages of each identified morphology in empty PNP, PAX-PNP and DiI-PNP samples under the various flow conditions including bulk preparation. As shown in Figure 4, the different preparation conditions result in different mixtures of spheres, cylinders, and vesicles. We define two types of vesicles: (1) small vesicles (d < 100 nm) containing a distinct small spherical compartments (SVs) and (2) large vesicles (d > 100 nm) containing either large spherical compartments or mixtures of smaller spherical and cylindrical compartments (LVs). For all three cases of hydrophobic molecule encapsulation (empty, PAX and DiI), we found that the highest percentage of SVs occurred at Q = 50 μL/min, while cylinders only appeared at Q = 200 μL/min (Figure 4 and Table 1). At each of the four flow conditions, the observed morphologies, their dimensions, and their percentages, are similar for the empty, PAX, and DiI cases (Table 1). We expect that the wide variation of size and shape observed in many of the nanoparticle samples will lead to heterogeneous

interactions and a complex range of nanoparticle behaviors in cell cultures. However, despite the observed sample polydispersity, we will show that average quantities describing PNP-cellular interactions, including EC_{50} values and rates of cell uptake, can be well correlated to simple average structural parameters such as mean hydrodynamic diameter.

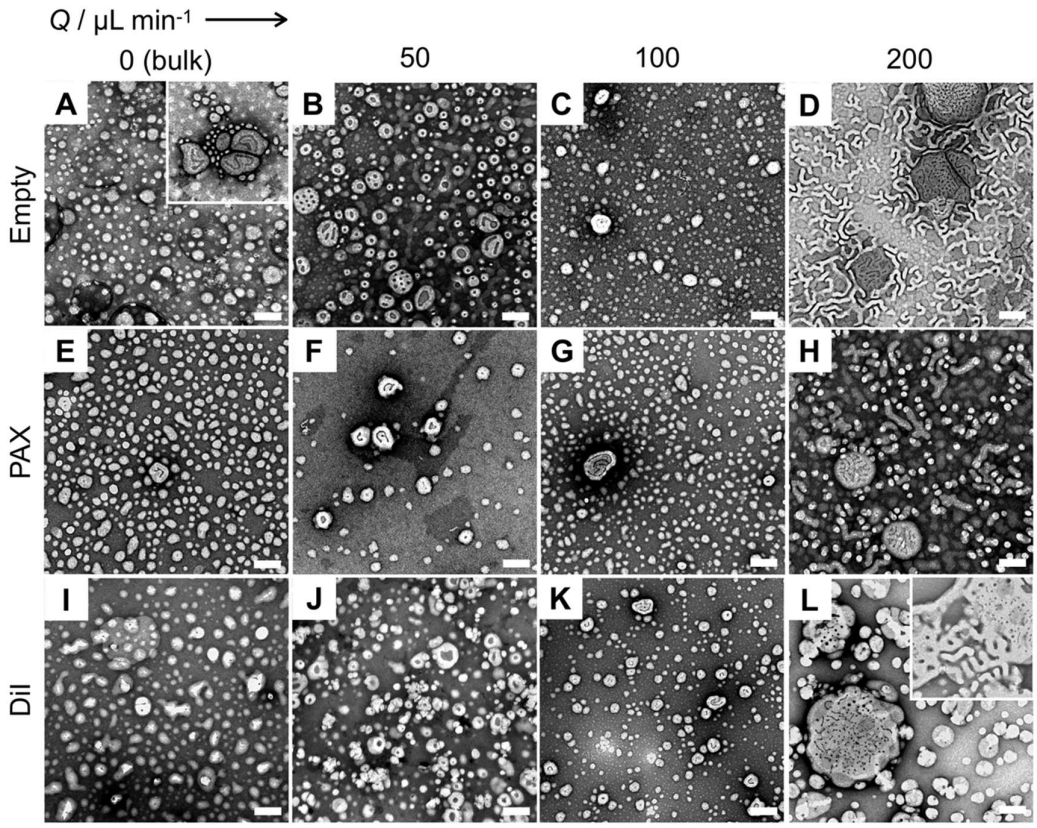

Figure 4. Representative TEM images of empty PNPs (A-D), PAX-PNPs (E-H), and DiI-PNPs (I-L) manufactured at various flow rates (Q = 50, 100, and 200 μL/min) using the microfluidic reactor or bulk nanoprecipitation (Q = 0 μL/min). Scale bars are 200 nm.

Table 1. Characteristics of PAX-PNPs and DiI-PNPs Manufactured at Variable Flow Rates.

Q / μL min^{-1}	Morphology[a]	Empty PNPs[c]		PAX-PNPs		DiI-PNPs	
		Dimension[b] / nm	Number Percentage / %	Dimension / nm	Number Percentage / %	Dimension / nm	Number Percentage / %
0 (bulk)	S	68 ± 5	98.5 ± 0.4	62 ± 1	97.5 ± 0.1	53 ± 3	91.2 ± 0.1
	SV	60 ± 4	1.1 ± 0.2	63 ± 4	0.2 ± 0.1	70 ± 3	4.3 ± 0.7
	LV	233 ± 12	1.4 ± 0.1	118 ± 5	0.6 ± 0.2	133 ± 2	4.5 ± 0.9
50	S	69 ± 9	79 ± 3	59 ± 3	75 ± 6	62 ± 1	76 ± 4
	SV	69 ± 5	18.1 ± 0.2	73 ± 4	13 ± 5	74 ± 1	14 ± 4
	LV	185 ± 15	3 ± 1	160 ± 5	13 ± 2	160 ± 20	11 ± 1
100	S	38 ± 4	99.5 ± 0.3	45 ± 3	98 ± 1	52 ± 1	96 ± 1
	SV	65 ± 7	0.5 ± 0.1	78 ± 3	1.1 ± 0.6	69.8 ± 0.1	0.96 ± 0.6
	LV	159 ± 15	0.5 ± 0.2	260 ± 20	0.6 ± 0.3	190 ± 40	2.6 ± 0.7
200	S	47 ± 4	55 ± 2	43 ± 2	58 ± 7	45 ± 9	62 ± 1
	SV	52 ± 10	1.5 ± 0.1	64 ± 5	6 ± 2	70 ± 7	8.3 ± 0.3
	LV	291 ± 81	2.3 ± 0.4	200 ± 40	7 ± 1	390 ± 80	7 ± 1
	C	31 ± 2	42 ± 3	37 ± 3	29 ± 5	38 ± 9	22 ± 1

[a]Morphologies are indicated as S (spheres), SV (small vesicles), LV (large vesicles), or C (cylinders). [b]Dimensions refer to sphere and small vesicle diameters and cylinder widths determined from TEM images. For non-spherical large vesicles, dimensions refer to the longest measurable internal distance. Standard errors are reported to represent the uncertainty of mean dimensions and number percentages determined from triplicate images in different regions of the TEM grid. [c]Empty PNP data are previously reported in ref. 55 and included here for comparison.

Microfluidic morphologies of DualM PNPs arise from a combination of kinetic and thermodynamic factors under variable shear conditions in the microfluidic channel.[55] The observed insensitivity of the morphologies to encapsulation of either PAX or DiI in the hydrophobic PNP regions (Table 1) suggests that neither molecule has a large effect on either chain mobility or local free energy within the PNPs at the

investigated drug loadings. This may be partly attributed to a relatively large free volume within the hydrophobic regions due to the long cleavable side chains of the PHMssEt block, providing space for hydrophobic molecules to intercalate without significant perturbations to chain mobility or dimensions. Another contributing factor may be the compressibility of the hydrophilic PEO compartments within vesicle morphologies. For example, as PAX or DiI is solubilized within the hydrophobic cores of SVs and LVs, expansion of the hydrophobic regions can be offset by compression of the hydrophilic compartments, preventing an increase in the chain packing stress that would trigger a morphological transition. Along with the consistent morphologies, this mechanism may also explains the consistent mean hydrodynamic sizes for the three different encapsulation cases described in the previous section.

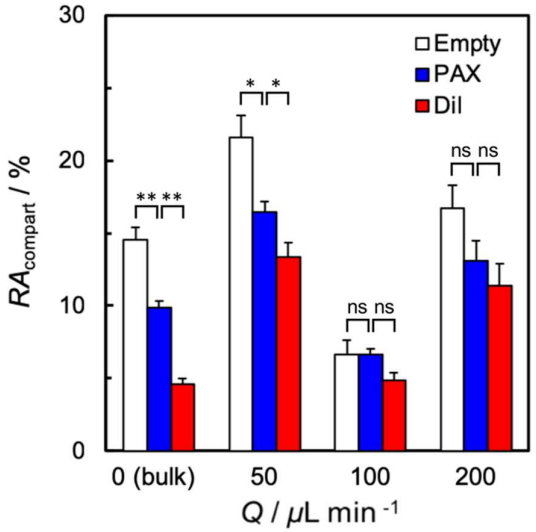

Figure 5. Relative areas of inner compartments, $RA_{compart}$, of empty PNPs (white), PAX-PNPs (blue), and DiI-PNPs (red) manufactured at various flow rates (Q = 50, 100, and 200 μL/min) using the microfluidic reactor or bulk nanoprecipitation (Q = 0

μL/min). Brackets indicate statistical comparisons between $RA_{compart}$ values: ** indicates $p < 0.005$, * indicates $p < 0.05$, and ns indicates $p > 0.05$.

We find evidence for compression of the hydrophilic compartments upon encapsulation of hydrophobic molecules by determining mean relative compartment areas $RA_{compart}$ from TEM image analysis of SVs and LVs. $RA_{compart}$ is a measure of the areal percentage of the internal dark area relative to the overall bright vesicle core area in the reverse-stained TEM images, which reflects the relative hydrophilic compartment volume of the cores. An example of the $RA_{compart}$ calculation is provided in *Supporting Information* (Figure S1). Figure 5 shows $RA_{compart}$ values determined for the three encapsulation cases (empty, PAX and DiI) under various flow conditions. $RA_{compart}$ values are generally lower in the PAX and DiI cases compared to the corresponding empty PNP case, providing evidence for compression of the hydrophilic compartments as SVs and LVs encapsulate hydrophobic molecules. Moreover, for each flow condition Figure 5 shows lower $RA_{compart}$ values in DiI-PNPs than in PAX-PNPs. This may be partly due to the more expanded molecular structure of DiI compared to PAX (Figure 1C), leading to greater swelling of hydrophobic domains and concomitantly greater compression of hydrophilic compartments. In addition, another contribution to lower $RA_{compart}$ values in DiI-PNPs may be the slightly higher loading of DiI compared to PAX as discussed in the next section.

Effect of Flow Rate on PAX and DiI Encapsulation Efficiencies in DualM PNPs. Figure 6 shows encapsulation efficiency (*EE*) and drug (or dye) loading (*DL*)

data for both PAX (blue data points) and DiI (red data points) encapsulation in DualM PNPs plotted as functions of flow rate (where Q = 0 μL/min indicates PNPs bulk preparation). For both encapsulated hydrophobic molecules, we find that *EE* (Figure 6A) values follow non-monotonic trends which approximately track with the flow rate dependencies of hydrodynamic PNP size (Figure 3A); for example, encapsulation of both PAX and DiI show maxima at Q = 50 μL/min (Figure 6A) where the hydrodynamic size also shows a maximum (Figure 3A). Plots of *EE* values for both hydrophobic molecules vs. the corresponding PAX-PNP or DiI-PNP $d_{h,eff}$ values from Figure 3A are shown in the inset to Figure 6A, along with best fit linear trend lines. The general increase in *EE* with increasing $d_{h,eff}$ values can be understood in terms of larger PNPs possessing hydrophobic domains of greater volume, allowing for encapsulation of larger numbers of hydrophobic molecules.[42]

DL values (Figure 6B) follow similar trends to the corresponding *EE* values (Figure 6A), although differences in *EE* with changes in Q are found to be statistically significant, whereas differences in *DL* with changes in Q are not found to be statistically significant. Under all flow conditions, DiI shows greater encapsulation than PAX (maximum *DL* = 7% and 4 %, respectively), suggesting generally higher solubility of DiI in the hydrophobic cores of DualM PNPs. We note that despite the solubility differences between the two drugs, the statistically significant differences in both DiI and PAX *EE* values at different flow rates (Figure 6A) indicate the pivotal role of microfluidic flow rate in encapsulation of both species.

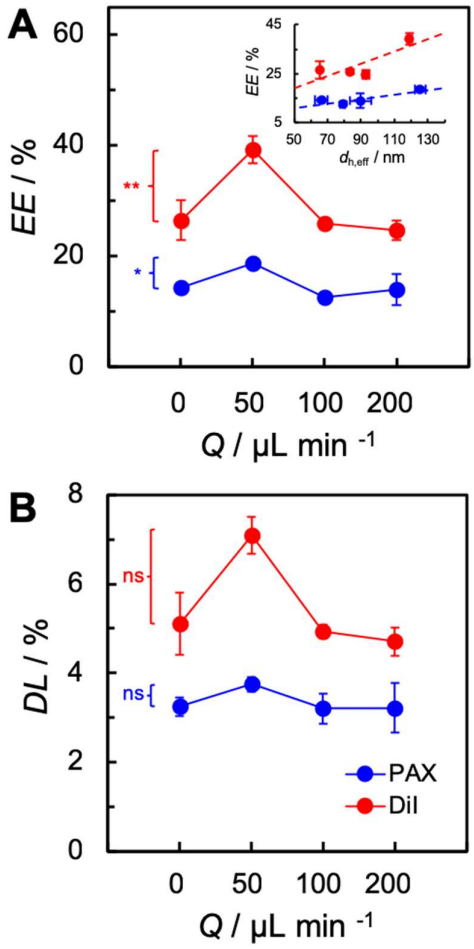

Figure 6. Encapsulation efficiency (*EE*, A) and drug loading (*DL*, B) of PNPs containing PAX (blue points) and DiI (red points) manufactured at various flow rates (Q = 50, 100, and 200 μL/min) using the microfluidic reactor or bulk nanoprecipitation (Q = 0 μL/min). Inset to (A) shows *EE* values vs. corresponding $d_{h,eff}$ values with best fit linear trend lines. Brackets indicate statistical comparisons between *EE* and *DL* values: ** indicates $p < 0.005$, * indicates $p < 0.05$, and ns indicates $p > 0.05$.

Taking advantage of the fluorescent properties of DiI, we were able to visualize and compare the homogeneity of dye molecule dispersion within the various PNP formulations. To do this, we merged fluorescence and optical microscopy images of

deposited films of DiI-PNPs prepared at the different flow conditions (Figure 7, A-D). Although the diffraction limit of optical microscopy does not allow individual PNPs to be resolved in these images, aggregates of PNPs are clearly visible as dark regions in the regular optical micrographs. Moreover, the overlap between red regions of DiI emission and dark regions of PNPs allows determination of the percentage of PNPs containing the fluorescent drug surrogate. Therefore, we propose defining encapsulation homogeneity (*EH*) as the mean area of overlapping red DiI regions divided by the mean area of dark PNP regions multiplied by 100%. The corresponding overlapping process from the merged images and a sample *EH* calculation is provided in *Supporting Information* (Figures S2 and S3, respectively).

From the series of image overlays, it is clear that a significant percentage of bulk-prepared PNPs do not contain DiI (Figure 7A) and that this percentage decreases considerably on the microfluidic chip (Figure 7B) and further still as the microfluidic flow rate is increased (Figure 7, C and D). This trend is represented by the increase in *EH* with increasing *Q* shown in Figure 7E. To our knowledge, this is the first example of microfluidic flow increasing the homogeneity of hydrophobic molecule encapsulation within PNPs. We tentatively attribute this effect to an increase in shear-induced particle coalescence and breakup events facilitating exchange and dispersion of DiI throughout the PNP population. The observed increase in *EH* associated with microfluidic manufacturing offers a significant advantage for nanomedicine

applications, since it decreases the number of therapeutically inactive PNPs, thus increasing the rate of targeted delivery to the tumor site.

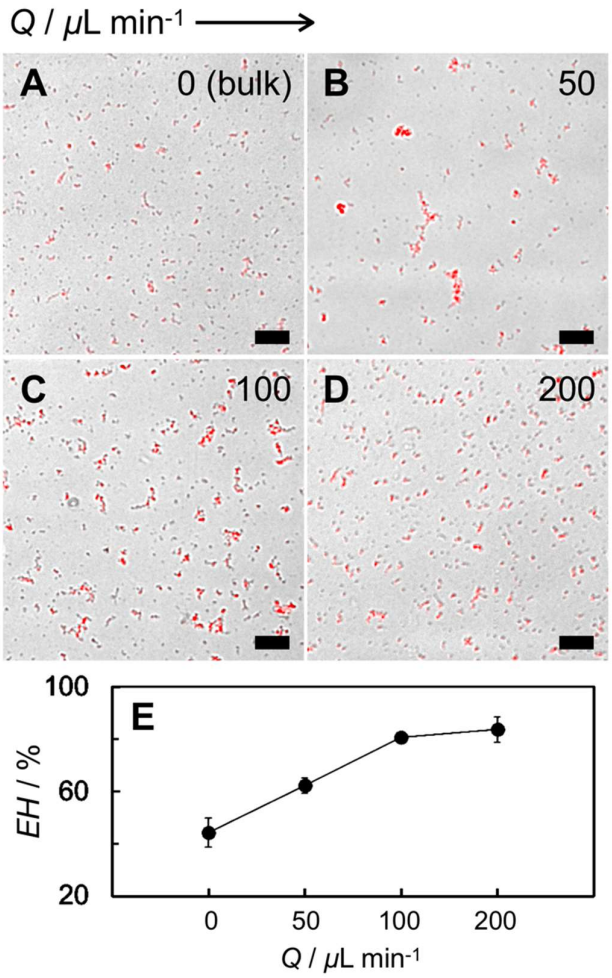

Figure 7. (A-D) Merged fluorescence and optical microscopy images of DiI-loaded PNPs manufactured at various flow rates (Q = 50, 100, and 200 μL/min) using the microfluidic reactor or bulk nanoprecipitation (Q = 0 μL/min). Scale bars are 20 μm. (E) Encapsulation homogeneity (*EH*) of the DiI-loaded PNPs.

Effect of Flow Rate on GSH-Triggered Release of PAX-Loaded DualM PNPs.

The *in vitro* PAX release kinetics were investigated for PAX-PNPs manufactured under the various flow conditions. Release experiments were conducted at 37 ºC under perfect

sink conditions using release media consisting of either PBS + 10 mM GSH or PBS with no GSH (control). Figure 8A shows the resulting PAX release profiles and associated fits of various PAX-PNPs. The first observation from these profiles is clear evidence of GSH-triggered release for all investigated PAX-PNP formulations, with PNPs in GSH medium releasing ~100% of their encapsulated PAX after 48h (solid circles), compared to PNPs in PBS which released only 40-50% of their PAX over the same time period (open circles).

Second, the GSH-triggered release kinetics in Figure 8A (solid fit lines) are clearly tunable with different flow conditions, with the bulk sample (black line) showing the fastest PAX release and the Q = 50 μL/min microfluidic sample (red line) showing the slowest release. Release half times ($t_{1/2}$) determined from the fits are plotted vs. flow rate in Figure 8B, showing a similar non-monotonic trend (i.e. an increase followed by a decrease) to hydrodynamic diameters (Figure 3A); the associated plot of $t_{1/2}$ vs. $d_{h,eff}$ is found to yield an approximately linear trend (Figure 8B, inset). The positive correlation between release half times and PNP size is explained by a combination of longer PAX and GSH diffusion distances within the cores of larger PNPs.

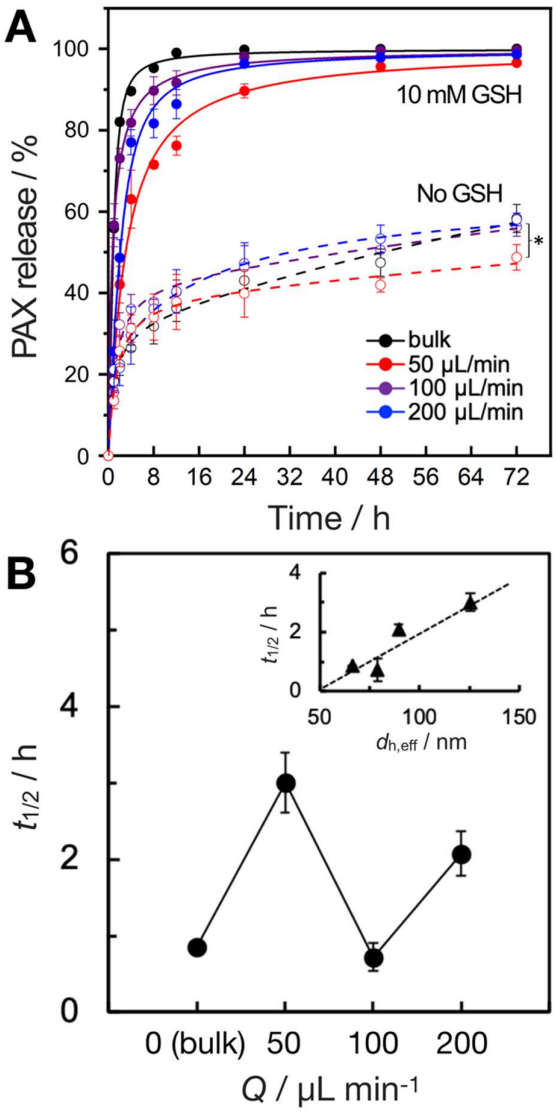

Figure 8. (A) PAX release profiles of PAX-PNPs manufactured at various flow rates (Q = 50, 100, and 200 μL/min) using the microfluidic reactor or bulk nanoprecipitation (Q = 0 μL/min). Solid circles represent PAX-PNPs incubated with GSH with solid lines showing associated fits; open circles represent PAX-PNPs incubated without GSH with dashed lines showing associated fits. The bracket indicates statistical comparisons between PAX release percentage values (without GSH) of the Q = 50 μL/min formulation and each of the other three formulations: * indicates $p < 0.05$. (B) Release half times ($t_{1/2}$) of PAX-PNP formulations (with GSH) vs. the flow rate, Q. The inset shows a plot of $t_{1/2}$ vs. $d_{h,eff}$ with linear regression trend line.

Finally, Figure 8A demonstrates that along with controlling GSH-triggered release profiles, microfluidic flow rate also provides some control for lowering the extent of diffusional release in the absence of GSH. Non-triggered diffusional release of drugs from PNPs in the body or under *in vitro* perfect sink conditions is driven by differential chemical potential of drug inside and outside the PNP. For example, all PNP formulations in the absence of GSH release ~55% of their PAX after 72 h, with the notable exception of the Q = 50 μL/min formulation, which releases only ~45% of its PAX over the same time period. This relative attenuation of non-triggered diffusional release for the Q = 50 μL/min sample results in a greater *difference* between GSH and non-GSH release at the 72 h time point (~55%) compared to the other formulations (~45%). Diffusional release of drug in the absence of GSH should be attenuated as much as possible in clinical applications to decrease side effects caused toxic exposure of healthy tissue and to increase drug delivery to the cancerous tumor. Therefore, the current results suggests that appropriate selection of flow conditions in future studies could be used to produce stimuli-responsive nanocarriers that maximize the percentage of injected drug delivered selectively to the tumor site.

We were interested in determining the relationships between GSH-triggered PAX release and associated GSH-triggered structural changes in PAX-PNPs due to cleavage of disulfide linkages. We therefore monitored both structural parameters $d_{\mathrm{h,eff}}$ and RA_{compart} over the first 24 h of the release experiments under release conditions with and without GSH (*Supporting Information*, Figures S4 and S5, respectively). Also shown

in *Supporting Information* are TEM images of PAX-PNPs at different time points during the first 24 hours of PAX release under GSH (Figure S6) and non-GSH (Figure S7) conditions. We find measurable increases in both $d_{\mathrm{h,eff}}$ and RA_{compart} during the first 24 h of PAX release under both sets of conditions, although for most formulations these changes are significantly greater in the presence of GSH, confirming the important role of GSH-triggered cleavage of disulfide linkages. Since the most rapid concurrent changes in PAX release, $d_{\mathrm{h,eff}}$ and RA_{compart} in the presence of GSH occur in the first four hours, we plot the changes in these three parameters over this time period in Figure 9A, 9B, and 9C, respectively. From these three plots, we calculated the following average rates for the first four hours of GSH-triggered PAX release:

$$R_{\mathrm{rel}} = \frac{\mathrm{PAX\ released_{4h} - PAX\ released_{0h}}}{4\ \mathrm{h}} \qquad (1)$$

$$R_{d\mathrm{h}} = \frac{d_{\mathrm{h,eff,4h}} - d_{\mathrm{h,eff,0h}}}{4\ \mathrm{h}} \qquad (2)$$

$$R_{RA} = \frac{RA_{\mathrm{compart,4h}} - RA_{\mathrm{compart,0h}}}{4\ \mathrm{h}} \qquad (3)$$

The insets to Figure 9B and 9C show plots of R_{rel} vs. $R_{d\mathrm{h}}$ and R_{rel} vs. R_{RA}, respectively, showing approximately linear correlations in both cases. These relationships indicate that GSH-triggered drug release tracks with GSH-triggered structural changes ($d_{\mathrm{h,eff}}$ and RA_{compart}) previously ascribed to cleavage of junction and pendant linkages, respectively,[55] suggesting contributions of both reactions to triggered drug release.[31]

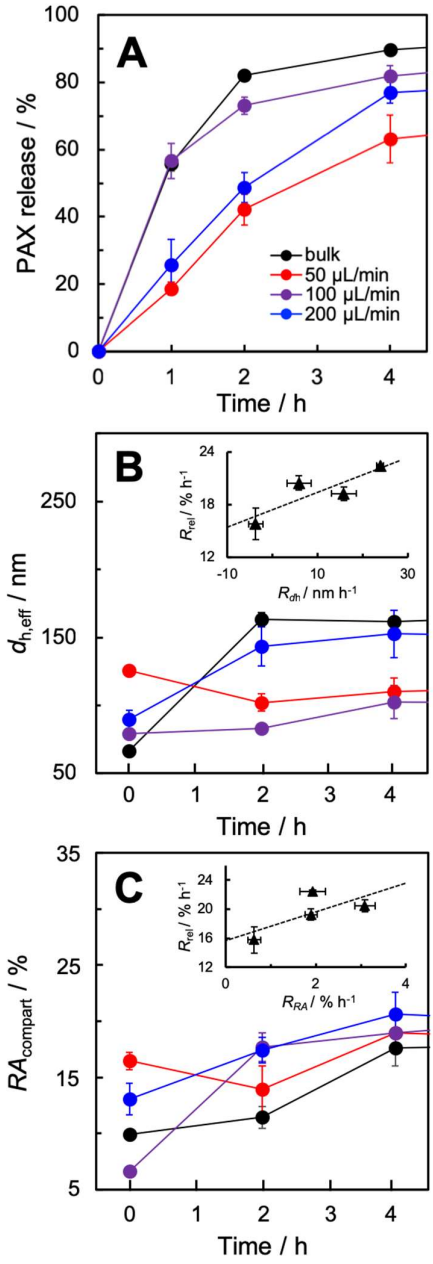

Figure 9. (A) PAX release percentage, (B) $d_{h,eff}$, and (C) $RA_{compart}$ values over the first four hours of release experiments in GSH. All plots show data for PAX-PNPs manufactured at various flow rates (Q = 50, 100, and 200 μL/min) using the microfluidic reactor or bulk nanoprecipitation (Q = 0 μL/min). Average rates of change of PAX release, $d_{h,eff}$, and $RA_{compart}$ (R_{rel}, R_{dh}, R_{RA}, respectively) over the four hours

were calculated from plots in (A), (B), and (C), respectively. Insets to (B) and (C) show plots of R_{rel} vs. R_{dh} and R_{rel} vs. R_{RA}, respectively, with linear fits.

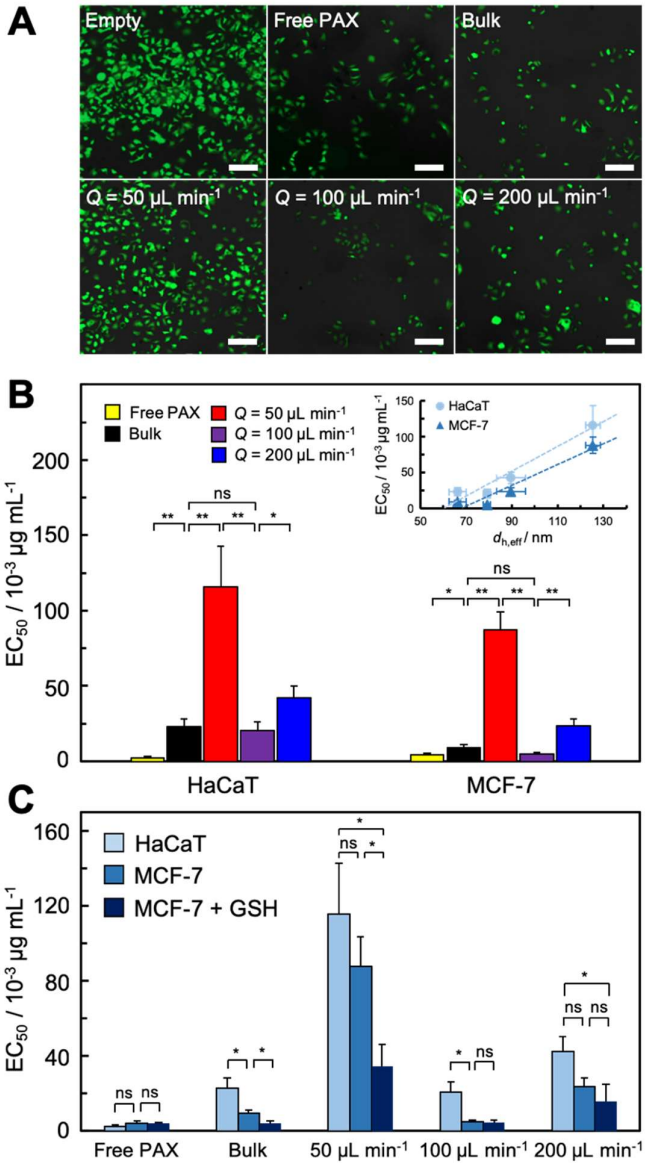

Figure 10. (A) Fluorescence images of MCF-7 cells treated with empty DualM PNPs, free PAX, and PAX-PNPs manufactured at various flow rates (Q = 50, 100, and 200 μL/min) using the microfluidic reactor or bulk nanoprecipitation (Q = 0 μL/min). Equivalent PAX concentrations are 0.1 μg/mL. Scale bars are 20 μm. (B) EC_{50} values of free PAX and PAX-PNP formulations for HaCaT (healthy) and MCF-7 (cancerous) cells. Inset shows linear relationships between both sets of EC_{50} values and PAX-PNP

$d_{h,eff}$ values. (C) Comparison of EC_{50} values for HaCaT, MCF-7, and MCF-7 + GSH. Incubation times were 48 h. Brackets indicate statistical comparisons between EC_{50} values: ** indicates $p < 0.005$, * indicates $p < 0.05$, and ns indicates $p > 0.05$.

Effect of Flow Rate on Cytotoxicity of PAX-Loaded DualM PNPs. We next investigated the cytotoxicity of DualM PAX-PNP formulations by comparing the responses of HaCaT (healthy) and MCF-7 (cancerous) cells to PAX-loaded PNPs manufactured using the microfluidic reactor at various flow rate (Q = 50, 100, and 200 μL/min) or using bulk nanoprecipitation (Q = 0 μL/min). MCF-7 is a well-studied breast cancer cell line that responds to many different anticancer agents including PAX; HaCaT cells are spontaneously transformed keratinocytes that are easily cultured non-cancerous control cells. We find that the empty DualM PNPs (including any remaining DMF in the dispersion following dialysis) do not show significant cytotoxicity to either HaCaT or MCF-7 cells within the investigated range of copolymer excipient concentrations (*Supporting Information*, Figures S8 and S9, respectively). Figure 10A qualitatively shows the cytotoxicity of free PAX and various PAX-PNPs to MCF-7 cells. Fluorescein diacetate selectively stains living cells which emit fluorescence in the green channel of the microscope. Therefore, by comparing the living cell densities in the images at equivalent PAX dosing levels, we find that microfluidic PAX-PNPs manufactured at Q = 50 μL/min show the lowest cytotoxicity (with the exception of the empty PNP control) whereas microfluidic PAX-PNPs manufactured at Q = 100 μL/min and bulk PAX-PNPs show the highest cytotoxicities (with the exception of free PAX).

More quantitative insights are obtained by analyses and comparison of cell viability data for free PAX and various PAX-PNP formulations over a range of PAX dosing amounts (*Supporting Information*, Figures S10-S13). Half maximal effective concentrations (EC_{50}) were determined from fits of 48 h cell viability plots for both HaCaT and MCF-7 cell lines, as shown in *Supporting Information* (Figures S10-S13); the resulting EC_{50} values are shown in Figure 10B. In general, encapsulation in PNPs decreases cytotoxicity (increases EC_{50} values) in cell cultures as drug availability is attenuated by encapsulation in the hydrophobic cores.[51,52] Moreover, variation in EC_{50} values between different PNP formulations demonstrates tunability of PNP-cell interactions *via* processing control of PNP size and shape. Both cell lines afford EC_{50} values with strong dependencies on the preparation method (bulk vs. microfluidic) and on the microfluidic flow rate. In fact, the following similar trend in EC_{50} values is found for both cell lines: Q = 50 μL/min > Q = 200 μL/min > Q = 100 μL/min ≈ bulk > free PAX. We note that this trend tracks well with the trend in PAX-PNP hydrodynamic sizes, as shown by the linear relationships between HaCaT and MCF-7 EC_{50} values and PAX-PNP $d_{h,eff}$ values (Figure 10B, inset). This suggests that microfluidic shear control leading to smaller PAX-PNP sizes results in formulations that are more cytotoxic to both healthy and cancerous cells.

Figure 10C compares EC_{50} values at each flow rate for three different cell environments: 1. HaCaT cells, 2. MCF-7 cells, and 3. MCF-7 cells pre-treated with 10 mM GSH-OEt, which can induce an increase of cellular GSH concentration (MCF-7 +

GSH).[56] Importantly, we find differential cytotoxicity between the two different cell lines, with higher EC_{50} values for HaCaT cells (lower cytotoxicity) than for MCF-7 cells (higher cytotoxicity) in each case of PAX-loaded DualM PNPs. For PNP formulations with the two highest EC_{50} values (Q = 50 and 200 μL/min), the measured differences between the HaCaT and MCF-7 cells are not significant due to statistical errors. However, the PNP formulations with the two lowest EC_{50} values (bulk and Q = 100 μL/min) are found to be significantly more cytotoxic to cancerous MCF-7 than to healthy HaCaT cells. This is in contrast to the free, unencapsulated PAX, which showed no significant difference between EC_{50} values for cancerous and healthy cells. These results indicate that encapsulation of PAX in DualM PNPs increases selectively between healthy (HaCaT) and cancerous (MCF-7) cells. Moreover, we find that this selectivity is also tunable *via* microfluidic flow. Defining selectivity as:

$$\text{Cytotoxic Selectivity} = \frac{EC_{50}(\text{HaCaT}) - EC_{50}(\text{MCF-7})}{EC_{50}(\text{HaCaT})} \times 100\% \qquad (4)$$

we find the greatest cytotoxic selectivity for the Q = 100 μL/min formulation (~76%), which has the smallest PNP size of the microfluidic formulations ($d_{h,eff}$ = 79 nm) and the lowest cytotoxic selectivity for the Q = 50 μL/min formulation (~24%), which has the largest size ($d_{h,eff}$ = 125 nm). This suggests that the current microfluidic approach provides a convenient manufacturing handle on optimizing DualM PNP selectivity for cancer cells *via* the flow tunability of $d_{h,eff}$ described in Figure 3A.

To further support the hypothesis that the selectivity of DualM PNP formulations is due to elevated GSH concentrations found in cancerous cells, we also tested free PAX and PAX-PNP formulations against MCF-7 cells that had been pre-treated with GSH-OEt to further increase GSH concentrations relative to intrinsic levels (MCF-7 + GSH) Cell viability data for empty PNPs, free PAX and PAX-PNPs in the MCF-7 + GSH environment are shown in *Supporting Information* (Figures S14-S16) and the resulting EC_{50} values are presented in Figure 10C. Importantly, GSH-OEt pre-treatments did not show significant toxicity to MCF-7 cells (*Supporting Information*, Figure S17), nor did the increase in GSH concentration show any difference in the cytotoxicity of free PAX (Figure 10C). However, each of the DualM PNP formulations showed a noticeable decrease in EC_{50} values against the MCF-7 + GSH cells compared to native MCF-7 cells, with these decreases being statistically significant in two of the four formulations. This provides good evidence that DualM PNP formulations show enhanced cytotoxicities in cellular environments with elevated GSH concentrations. In fact, the combined effects of GSH concentration and flow rate shown in Figure 10C suggest that different manufacturing conditions leads to variable thresholds for GSH responsivity. Specifically, both bulk and Q = 100 μL/min PAX-PNP formulations showed GSH thresholds for increased cytotoxicity relative to HaCaT cells that were at or below the intrinsic GSH levels in MCF-7. On the other hand, the Q = 50 μL/min and Q = 200 μL/min PAX-PNP formulations showed higher GSH thresholds for increased

cytotoxicity relative to HaCaT cells, with these thresholds being between the intrinsic MCF-7 GSH levels and the elevated GSH levels in pre-treated MCF-7.

Effect of Flow Rate on MCF-7 Cell Uptake Rates of DualM PNPs. In Figure 8B, we showed a linear correlation between GSH-triggered PAX release half times and particle size (Figure 8B), with smaller PNP sizes leading to faster PAX release. This relationship may partly explain the linear increases in EC_{50} values with increasing particle size (Figure 10B), since slower PAX release in the cell medium would cause lower cytotoxicity (higher EC_{50} values). However, another possible contribution of particle size to cytotoxicity is the rate of cell uptake of PNPs, since release of PAX within the cell would have a greater cytotoxic effect than release of PAX in the extracellular matrix of the tumor. To investigate cell uptake qualitatively, we used fluorescence microscopy to visualize DAPI-stained MCF-7 cells that had been incubated with various DiI-PNP formulations for 2h. In these experiments, the DiI dye served as a fluorescent surrogate for non-fluorescent PAX, based on the result that sizes and morphologies of PAX-PNP and DiI-PNP are similar for all manufacturing conditions (Figures 3 and 4). Figure 11 shows the resulting fluorescence images of MCF-7 uptake of DiI-PNPs. In each image, the DAPI (blue regions) indicate the cellular nuclei while the DiI (red regions) indicate the PNPs. From the images of merged DAPI and DiI channels, the Q = 100 μL/min formulation appears to show the highest extra-nuclear compartmentalization of DiI (Figure 11K), while the Q = 50

μL/min and 200 μL/min formulations show the lowest extra-nuclear compartmentalization of DiI (Figure 11, J and L, respectively).

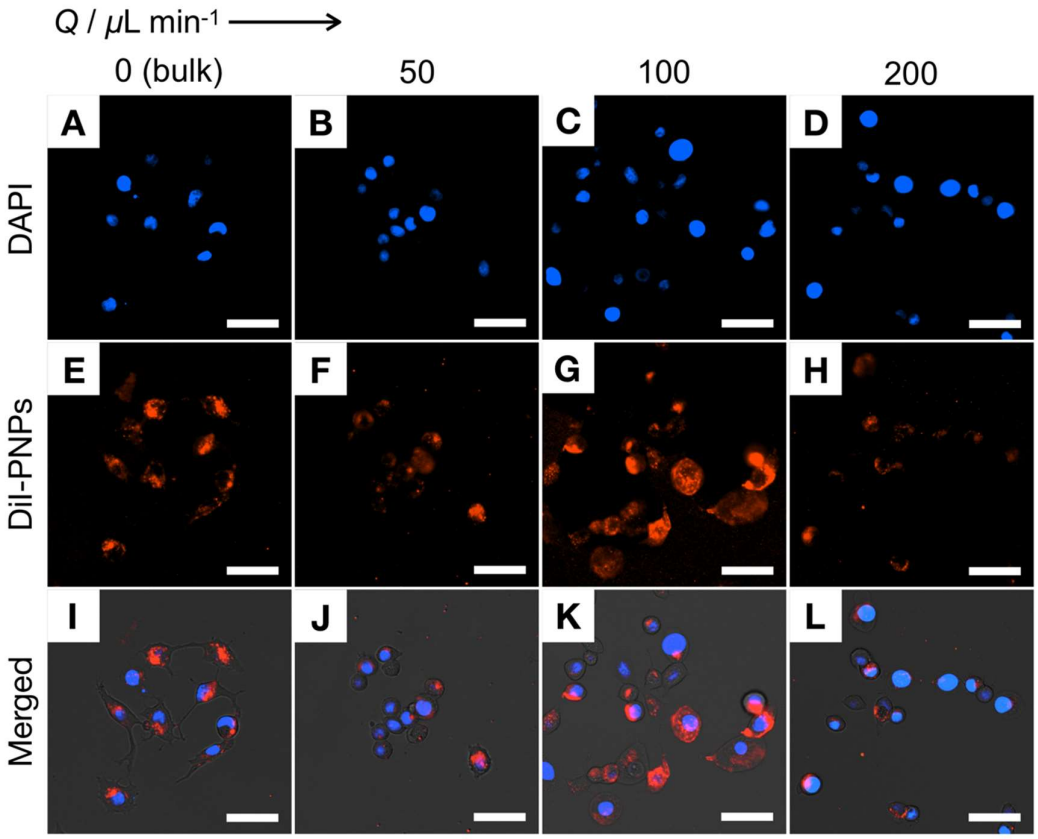

Figure 11. Fluorescence images of DAPI-stained MCF-7 cells treated with DiI-PNPs manufactured at various flow rates (Q = 50, 100, and 200 μL/min) using the microfluidic reactor or bulk nanoprecipitation (Q = 0 μL/min). (A−D) DAPI channel (blue) indicating locus of nuclei; (E−H) DiI channel (red) indicating locus of Di-PNPs; (I−L) merged images combining DAPI (blue) and DiI (red) channels. Scale bars are 20 μm.

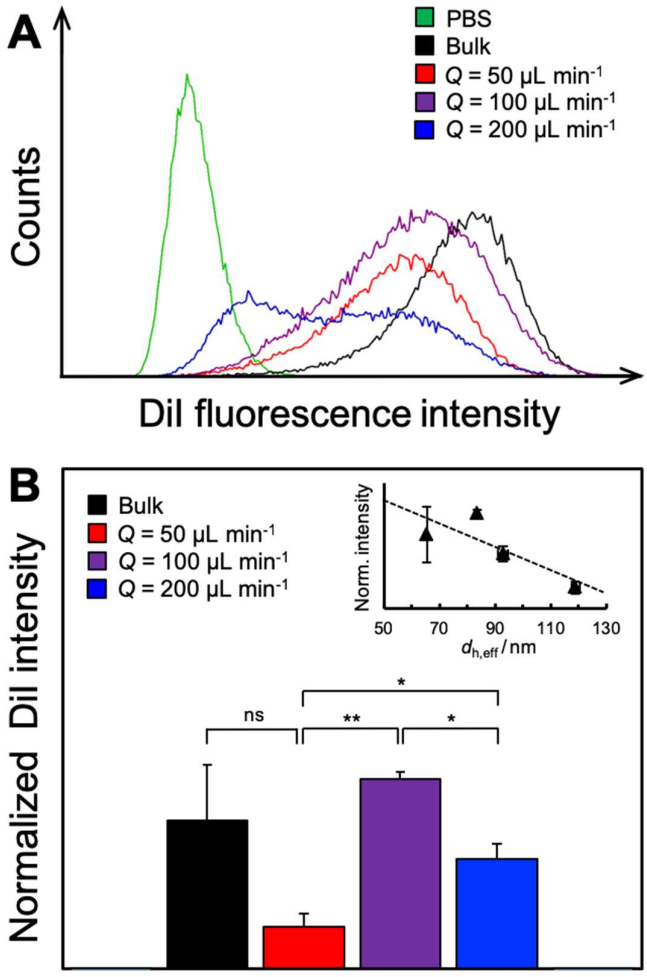

Figure 12. (A) Histograms of DiI fluorescence intensity from MCF-7 cells treated with DiI-loaded PNPs manufactured at various flow rates (Q = 50, 100, and 200 µL/min) using the microfluidic reactor or bulk nanoprecipitation (Q = 0 µL/min). (B) Normalized fluorescence intensities of MCF-7 cells treated with various DiI-loaded PNP formulations. The inset plots normalized fluorescence intensities of MCF-7 cells vs. mean effective hydrodynamic diameters of the PNPs showing a negative linear correlation. Brackets indicate statistical comparisons between normalized fluorescence intensities: ** indicates $p < 0.005$, * indicates $p < 0.05$ and ns indicates $p > 0.05$.

Based on fluorescence images such as those in Figure 11, it is difficult to quantify differences in cell uptake related to flow rate. Therefore, to quantify cell uptake, we

carried out flow cytometric measurements of the MCF-7 cells following incubation with the various formulations. Figure 12A shows the resulting DiI fluorescence intensity histograms of MCF-7 cells treated with different DiI-PNPs (gating strategy is shown in *Supporting Information,* Figure S18). As a negative control, cells treated with same volume of PBS but no DiI-PNPs were also measured (PBS, green histogram). For all cell populations treated with DiI-PNPs, we observe clear shifts to higher DiI intensities relative to the control group, confirming association of DiI-PNP with MCF-7 cells for all nanoparticle formulations. Based on the fluorescence microscopy data in Figure 11, and also on the likelihood of any surface-bound DiI-PNPs being removed during cell washing, we attribute cellular association of DiI-PNPs to their extra-nuclear compartmentalization. Therefore, to elucidate the relative cell uptake of the various DiI-PNP formulations, normalized DiI intensity values for each formulation were obtained by integrating mean fluorescence intensity values (*Supporting Information*, Figure S19) and dividing by the dye loading (*DL*) of the corresponding DiI-PNP sample (Figure 6B). The resulting normalized values (Figure 12B) provide a relative measure of the rate of PNP uptake into MCF-7 cells, showing the greatest uptake by the $Q = 100$ μL/min formulation (purple bar) and the lowest uptake by the $Q = 50$ μL/min formulation (red bar). Plotting normalized DiI intensity vs. the $d_{h,eff}$ values of the corresponding DiI-PNPs (Figure 3A) yields a negative linear relation (Figure 12B, inset), indicating greater uptake rates for PNPs of smaller size. We conclude that as PNP sizes decrease *via* microfluidic shear processing, *both* increased drug release rates

(Figure 8B) *and* increased cell uptake (Figure 12B) will contribute to the observed increases in cytotoxicities against MCF-7 cells (Figure 10B, inset).

Conclusions

Polymer nanoparticles (PNPs) providing encapsulation of anticancer drugs with selective stimuli-responsive release at tumor sites are promising candidates in the development of smart nanomedicines. In this paper, we employed a two-phase microfluidic reactor to produce DualM PNPs consisting of a glutathione (GSH)-responsive block copolymer with disulfide linkages at both the hydrophobic-hydrophilic junction and on pendant groups in the hydrophobic block and containing either the anticancer drug paclitaxel (PAX) or the fluorescent drug surrogate dye (DiI). We show that on-chip self-assembly at different flow rates yielded DualM PNPs with different flow-controlled sizes, structures, and drug delivery function. Sizes and morphologies of PAX-loaded and DiI-loaded PNPs were found to be similar to empty PNPs under the same flow conditions, providing opportunities for controlled loading of different therapeutics with different molecular structures. Using fluorescence imaging of the DiI probe dye, we show that microfluidic self-assembly improves encapsulation homogeneities within PNPs relative to bulk nanoprecipitation, with further improvements as the flow rate increases. PAX-loaded DualM PNPs were shown to be significantly more toxic to cancerous MCF-7 cells (lower EC_{50} values) than to healthy HaCaT cells, while free (not encapsulated) PAX showed similar toxicity to both

cell lines, supporting the biological responsivity and selective nature of the nanocarriers. Interestingly, the specific drug delivery properties of the DualM PNP formulations were tunable with microfluidic flow rate, with several properties, including GSH-triggered release rate, MCF-7 cell uptake, cytotoxicity, and relative difference in MCF-7 and HaCaT cytotoxicity, increasing linearly as flow-directed PNP size decreased. These various linear size-property relations suggest that nanoparticle hydrodynamic diameter, conveniently tunable *via* microfluidic flow rate, is a key structural factor influencing numerous important delivery properties for biologically-responsive nanoparticles. These results highlight the potential of flow-directed shear processing in two-phase microfluidic reactors for providing controlled manufacturing routes to biological stimuli-responsive nanomedicines optimized for specific therapeutic applications.

Experimental

Materials. The PEO-ss-PHMssEt block copolymer with a number-average molecular weight of M_n = 29 000 g/mol and a dispersity of $Đ$ = 1.12 was synthesized and characterized as described in detail in a recent publication.[31] Paclitaxel (PAX, >99.9%) was purchased from PolyMed Therapeutics. L-glutathione (GSH, >98%), glutathione reduced ethyl ester (GSH-OEt, ≥90%), and 1,1′-dioctadecyl-3,3,3′,3′-tetramethylindocarbocyanine perchlorate (DiI) purchased from Sigma-Aldrich, *N*,*N*-dimethylformamide (DMF, >99.9%), acetonitrile (HPLC grade), and dimethyl sulfoxide (DMSO, ≥99.9 %) from Fisher Scientific was used as received

without further purification. NaCl (BioBasic Canada, 99.9%), KCl (Caledon, 99.0%), Na_2HPO_4 (BioBasic Canada, 98.0%), and KH_2PO_4 (Caledon, 99.0%) were used to prepare phosphate-buffered saline (PBS, pH=7.4).

Bulk Preparation of Drug-Loaded DualM PNPs. The DualM PNPs containing drug (PAX) or dye (DiI) were first prepared by the conventional bulk method of nanoprecipitation described in detail in our previous publication.[55] Specifically, ~1 g of 0.33 wt % copolymer in DMF stock solution containing a drug (or dye)-to-polymer ratio (w/w) of r = 0.25 was prepared and stirred overnight. This solution was added at a constant injection rate (120 μL/min) using a syringe pump into a 10× excess volume of deionized water with vigorous stirring. The resulting dispersion was dialyzed to remove residual DMF,[55] then the aqueous sample was centrifuged (16,000×g for 10 min) to remove unencapsulated drug (or dye).[55] Bulk samples were prepared in triplicate and were analyzed immediately following dialysis.

Microfluidic Reactor Fabrication. The microfabrication steps followed previously described procedures[43-55] and details of the methodology can be found in our previous publication.[55] In brief, negative masters on silicon wafers (Silicon Materials) were fabricated using the negative photoresist SU-8 100 (Microchem). Then, polydimethylsiloxane (PDMS) microfluidic chips were fabricated from the masters using a SYLGARD 184 silicon elastomer kit (Dow Corning). The resulting reactor (Figure 2) has a set channel depth of 150 μm, with a sinusoidal mixing channel 100 μm wide and a sinusoidal processing channel 200 μm wide.[43-55]

Flow Delivery and Control. The steps of flow delivery and control followed previously described procedures.[55] In brief, microfluidic flow of liquids was provided using 1 mL gastight syringes (Hamilton) mounted on syringe pumps (Harvard Apparatus). Argon (Ar) gas flow within the microfluidic channels was provided *via* an Ar tank regulator and a downstream regulator (Johnston Controls). The liquid flow rate (Q_{liq}) was programmed *via* the syringe pumps, and the gas flow rate (Q_{gas}) was adjusted *via* the downstream pressure regulator in order to set the nominal total flow rate. Actual values of Q_{gas}, Q_{gas}/Q_{liq}, and $Q_{total} = Q_{gas} + Q_{liq}$ were calculated from the average volume of gas bubbles in the microchannels (*Supporting Information*, Tables S1 and S2).[55] Images of the microchannels were captured using a Genie Nano-C1280 camera (1stVision) equipped with an On-Semi Python1300 sensor and a C-Mount Manual Iris Varifocal lens (1/1.8", 4-13mm, *f*/1.5) (Tamron) and analysis of the gas bubbles was achieved using image analysis software (ImageJ). All actual Q_{total} values within Tables S1 and S2 are within 10 % of nominal Q values.

Microfluidic Preparation of Drug-Loaded DualM PNPs. For microfluidic preparation of drug-loaded DualM PNPs, the following three fluid streams were combined to give stable gas-segmented liquid plugs within the reactor, (1) 1.0 wt % copolymer in DMF solution with a drug (or dye)-to-polymer ratio (w/w) of $r = 0.25$ (PAX or DiI); (2) pure DMF; and (3) DMF/water. The flow rates of the three liquid streams were equal for all runs, and the water content of the DMF/water stream was selected to yield steady-state on-chip concentrations of 0.33 wt % copolymer and 21.7

wt % water. The critical water content of 0.33 wt % copolymer in DMF was previously determined to be 11.7 ± 0.2 wt %,[55] so that the water content for microfluidic DualM PNP preparation is designated cwc + 10 wt % for all investigated flow rates. After microfluidic mixing, the PNPs were collected from the chip into vials containing 10× excess by volume of deionized water. The resulting dispersion was dialyzed to remove residual DMF,[55] then the aqueous sample was centrifuged (16,000×*g* for 10 min) to remove unencapsulated drug (or dye).[55] Microfluidic samples at each flow rate were prepared in triplicate and were analyzed immediately following dialysis.

Determination of DualM PNP Encapsulation Efficiencies. For each PAX-loaded PNP sample, ~1 g of a gravimetrically determined quantity of dispersion was used for encapsulation efficiency (*EE*) and drug loading (*DL*) determination. Water was first removed by rotary evaporation for 15 min at 25 °C; then a known gravimetrically determined quantity of acetonitrile (~0.5 g) was added to dissolve the resulting solid film. The mixture was vortexed for 5 min first and stirred overnight at room temperature (22 °C) to ensure complete breakup of the PNPs and dissolution of the drug. High performance liquid chromatography (HPLC) (Agilent 1100) equipped with a Luna 5u C18 column (Phenomenex) and a diode array detector (DAD) set at 252 nm was used to quantify the drug concentration. 50 μL of the drug/acetonitrile solution was injected into the HPLC by an auto-sampler. The eluent consisting of acetonitrile and water (65:35, v/v) with 0.1 v% formic acid was run at 1 mL/min. The column temperature was kept at 25 °C during all measurements. A calibration curve for the DAD was

generated by analyses of 5 standards containing known PAX concentrations in acetonitrile. Quantities of PAX in the various dissolved PNP solutions were determined using the calibration curve.

For the *EE* and *DL* determination of DiI-loaded PNPs, 1 drop (~0.02 g of a gravimetrically determined quantity) of each sample was dissolved in a gravimetrically determined quantity of DMF (~5 g) then stirred overnight at room temperature (22 °C) in the dark. 200 μL of the resulting DiI/DMF solution was transferred into a 96-well chemically resistant microplate (Whatman Multi-Chem), and the fluorescence intensities of the samples were determined by a SpectraMax M5 microplate reader (Molecular Devices) at the emission maximum (λ_{ex} = 549 nm; λ_{em} = 565 nm). A linear fluorescence intensity-concentration calibration curve for DiI at the same excitation and emission wavelengths was also generated using 5 standards containing known DiI concentrations in DMF. The fluorescence readings for both standards and samples were obtained within 2 min and at 25 °C. The solvent background was subtracted for each sample and standard measurement. Quantities of DiI in the various dissolved PNP solutions were determined using the calibration curve.

EE and *DL* were calculated for each PAX- or DiI-loaded PNP sample using the following equations:

$$EE\ (\%) = \frac{\text{mass encapsulated drug}}{\text{total mass drug}} \times 100 \qquad (5)$$

$$r = \frac{\text{total mass drug}}{\text{total mass copolymer}} \times 100 \qquad (6)$$

$$DL\ (\%) = \frac{\text{mass encapsulated drug}}{\text{mass encapsulated drug+total mass copolymer}} \times 100 \qquad (7)$$

$$DL\ (\%) = \frac{r \times EE}{(r \times EE)+1} \times 100 \qquad (8)$$

Reported *EE* and *DL* values for each condition of *Q* was determined by averaging the values from triplicated preparations. Standard errors (σ) on *EE* and *DL* values were calculated from the standard deviation (*s*) of triplicate values: $\sigma = \frac{s}{\sqrt{3}}$.

Determination of Microfluidic Encapsulation Homogeneity. Fluorescence images of DiI-loaded PNPs were taken for encapsulation homogeneity (*EH*) analysis. 100 μL of each investigated aqueous dispersion of DiI-PNPs was transferred into a 96-well chemically resistant microplate (Whatman Multi-Chem), and the fluorescence images were captured using a Cytation5 microplate reader equipped with fluorescent microscope (BioTek), with fluorescent filter cubes of emission (nm)/excitation (nm) = 586/647. Images were taken using a 4× objective. Bright field/fluorescence merged images excluding any non-encapsulated DiI were processed by the imaging software. The red areal percentage relative to PNP areal percentage was analyzed using ImageJ. Briefly, the black areal percentage ($\%A_{\mathrm{PNP}}$) and red areal percentage ($\%A_{\mathrm{DiI}}$) of the merged image were measured using color threshold and measurement functions. The encapsulation homogeneity of DiI was then calculated:

$$EH(\%) = \frac{\%A_{\mathrm{DiI}}}{\%A_{\mathbf{PNP}}} \times 100 \qquad (9)$$

Reported *EH* values represent averages calculated from 9 images (3 images × triplicate preparations). Reported uncertainties σ were calculated from the standard deviation *s* of average values of triplicate preparations: $\sigma = \frac{s}{\sqrt{3}}$.

Dynamic Light Scattering. DLS measurements were performed on a Brookhaven Instruments ZetaPALS Analyzer at a temperature of 25 °C and a scattering angle of 90°.[55] PNP concentrations for DLS measurements were ~0.01 mg/mL. DLS analysis was carried out as described in our previous publication.[55] Reported uncertainties (σ) on hydrodynamic sizes and polydispersities were calculated from the standard deviation (*s*) of triplicate values: $\sigma = \frac{s}{\sqrt{3}}$.

Transmission Electron Microscopy. PNP samples for TEM analysis were prepared using uranyl acetate negative staining as described in our previous publication.[55] TEM was performed on a JEOL JEM-1400 instrument at an accelerating voltage of 80 kV.[55] Image analysis and size determinations were carried out using ImageJ. Methods of image analysis and statistics were identical to those described in our previous paper.[55] Reported uncertainties (σ) on particle dimensions were calculated from the standard deviation (*s*) of average dimensions determined from three images: $\sigma = \frac{s}{\sqrt{3}}$.

The relative areas of inner vesicle compartments were calculated as described in our previous paper:[55]

$$RA_{\text{compart}}\ (\%) = \frac{A_{\text{compart}}}{A_{\text{PNP}}} \times 100 \qquad (10)$$

Reported uncertainties (σ) on RA_{compart} were determined from the standard deviation (s) of relative areas for N measured PNPs: $\sigma = \frac{s}{\sqrt{N}}$.

The inner hydrophilic compartments of SVs and LVs appeared dark in TEM images due to reverse staining. This allowed spheres to be distinguished from vesicles, since the hydrophobic cores of spheres appeared uniformly bright while SVs and LVs contained one or more dark compartments. For SVs and LVs, the areal percentage of dark inner compartments relative to the entire particle area was analyzed using ImageJ. Briefly, a cropped image of each selected PNP was adjusted by selecting appropriate contrast, sharpness, and brightness levels. Then boundaries of the PNP and its internal compartments were defined using the binarization function of the software. Finally the total inner compartment area, A_{compart}, and the total PNP area, A_{PNP} were calculated by the software.

***In Vitro* Release Kinetics of PAX-Loaded PNPs.** Near perfect sink conditions were established for *in vitro* release experiments, and HPLC was used to monitor the PAX release kinetics of PAX-loaded PNPs. In a typical experiment, a gravimetrically determined quantity (~10 g) of PAX-loaded PNPs was transferred into a pre-conditioned Float-A-Lyzer dialysis tube (10 mL, MWCO 100 kDa, SpectrumLabs). The tube was then placed in a 2L-baker of the release medium. Two different release media were prepared: 1. ~2 L PBS with ~6.14 g GSH dissolved to reach 10 mM GSH concentration (GSH condition); 2. ~2L PBS only (no GSH condition). Throughout the release experiments, the release medium was constantly stirred at 100 rpm, and

maintained at physiological temperature (37 ± 0.2 °C). For each of the first seven pre-determined time points (t = 0, 1, 2, 4, 8, 12, and 24 h), 1 mL of the sample was transferred into a vial and weighed, while for each of the t = 48 and 72 h time points, 1.5 mL of the sample was transferred into a vial and weighed. At four time points (t = 0, 2, 4, and 24 h), 2 drops of the samples were also taken out for immediate DLS and TEM analyses. For samples used for PAX concentration determination, water was removed by rotary evaporation for 15 min at 25 °C. A known gravimetrically determined quantity of acetonitrile (~0.5 g) was added to dissolve the resulting solid film. The mixture was vortexed for 5 min first and stirred overnight at room temperature (22 °C) to ensure complete breakup of the PNPs and dissolution of the drug. Before injection into the HPLC, the samples were filtered through a Teflon syringe filter with 0.2 μm nominal pore size (Phenomenex). The PAX concentration was measured by HPLC as described in a previous section. Percentages of PAX released were calculated relative to the determined mass of PAX in PAX-PNPs at the t = 0 release time. Reported percentages of PAX released for each condition was determined by averaging the values from triplicate preparations. Standard errors (σ) are reported to represent the precision of the mean release percentages, which were calculated from the standard deviation (s) of triplicate values: $\sigma = \frac{s}{\sqrt{3}}$.

The release profiles for PNPs incubated under GSH conditions were plotted and fit using the following 2-parameter hyperbola model:

$$y = \left(\frac{1}{2B}\right)\left[(x + A) + B - \left((x + A) + B\right)^2 - (4xB)^{0.5}\right] \qquad (11)$$

Release profiles for PNPs incubated in pure PBS (no GSH) were plotted and fit using the 5-parameter hyperbola model:

$$y = \frac{Ax}{B+x} + \frac{Cx}{D+x} + E \qquad (12)$$

The fits were processed using the Levenberg−Marquardt algorithm within OriginLab (Version 2019b, OriginLab). Release half times, $t_{1/2}$, of the various PAX-PNP formulations under GSH conditions were then extracted by calculating the time required to achieve 50% PAX release based on the fitted curves. Experimental errors of $t_{1/2}$ were represented by standard errors (σ) derived from the goodness of fit.

Cell Culture. MCF-7 (human breast adenocarcinoma) cells were was purchased from ATCC, and HaCaT (human healthy keratinocyte) cells were obtained as a generous gift from Dr. Mohsen Akbari (Department of Mechanical Engineering, University of Victoria). MCF-7 and HaCaT cell lines were cultured to represent the environment of cancerous and healthy tissue, respectively. Both cell lines were cultured in Dulbecco's Modified Eagle's Medium (DMEM, Gibco) supplemented with 10% fetal bovine serum (FBS, YWR) and 1% antibiotics (penicillin and streptomycin) in 75 cm^2 tissue culture flasks and maintained at 37 °C with 5% CO_2 in a tissue culture incubator. The HaCaT and MCF-7 cells were sub-cultured periodically using 0.5% trypsin/EDTA (Gibco).

***In Vitro* Cytotoxicity of PAX-Loaded PNPs.** MCF-7 and HaCaT cells were grown to ~80% confluence in 75 cm^2 tissue culture flasks, then trypsinized, collected, and pelleted by centrifugation (5 min at 1,400 rpm). The cell pellet was then suspended in DMEM, and the cell concentration was determined using a hemocytometer. After the initial cell concentration was determined, the suspension was diluted to 1.0×10^5 cells/mL. Next, a mulitichannel pipette was used to fill a 96-well plate (Corning) with 100 μL/well of the diluted cell suspension. The plates were then incubated for 24 h at 37 °C with 5% CO_2 in a tissue culture incubator for cell adhesion.

According to measured drug loading levels, aqueous stock dispersions of each investigated sample of PAX-PNPs were mixed with DMEM, resulting in a 650 μL PNP/DMEM mixture with a working PAX concentration of 2 μg/mL. To prepare the free PAX solution, 6.5 μL of PAX dissolved in dimethyl sulfoxide (DMSO) were diluted in the 643.5 μL of DMEM media to obtain a working PAX concentration at 2 μg/mL. Serial dilutions were carried out, and then 100 μL of each diluted stock was added to the appropriate well of the 96-well plate (containing ~1.0×10^4 cells in 100 μL of DMEM, as described above), to generate a range of different concentrations for analysis (1, 0.308, 0.095, 0.029, 0.0090, 0.0028, and 8.5×10^{-4} μg/mL PAX). The treated cells were incubated for 48 h at 37 °C with 5% CO_2 in a tissue culture incubator. To determine cell viability, 40 μL of CellTiter-Blue (Promega) was added to each well after the predetermined incubation time, according to the manufacturer's instructions. After the addition of CellTiter-Blue, the 96-well plates were incubated for 4 h (37 °C

with 5% CO_2), and then fluorescence (λ_{ex} = 560 nm; λ_{em} = 590 nm) readings were recorded on a Cytation5 microplate reader (BioTek). Cell death was calculated for each well based upon the following formula:

$$\%\text{Death} = \left[1 - \frac{(S - B_0)}{(B_t - B_0)}\right] \times 100 \qquad (13)$$

where S is the sample reading (cells + drug + media), B_t is the average reading for the untreated population of cells (cells + media), and B_0 is the average reading of wells containing media only (media). %Death vs. PAX concentration data sets were fit using the following dose-response model:

$$y = A_1 + \frac{A_2 - A_1}{1 + 10^{p \log(x_0 - x)}} \qquad (14)$$

The data sets were processed by the Levenberg–Marquardt algorithm within OriginLab (Version 2019b, OriginLab), and by forcing fits through 0% death at low PAX concentrations. Reported EC_{50} values were determined from three separate PAX-PNP preparations, with each concentration of each preparation being tested 6 times. Standard errors (σ) were obtained from the goodness of fit for each EC_{50} plot and used to report error bars. These same σ were then used to calculate the p-values for determination of statistical significance in comparisons between measured EC_{50} results.

For visual representation of the cytotoxicity of PAX- PNPs against MCF-7 cells, the cells were seeded at a density of 2.0×10^5 cells per well in a 6-well plate (Costar) and allowed to incubate in 1 mL of DMEM (containing 10% FBS and 1% antibiotics, as described in the previous section) for 24 h at 37 °C with 5% CO_2 in a tissue culture

incubator for cell adhesion. According to measured drug loading levels, aqueous stock dispersions of each investigated sample of PAX-PNPs were mixed with DMEM, resulting in a PNP/DMEM mixture with a working PAX concentration at 0.1 μg/mL. After overnight incubation, cells were washed once with PBS and the media was replaced with 1 mL of the PNP/DMEM mixture. Cells were incubated for 48 h and then were washed twice with cold PBS. Fluorescein diacetate (F-7838F7378, Sigma-Aldrich) was dissolved at a concentration of 0.1 mg/mL in DMSO and further diluted 100-fold in PBS to afford a final concentration of 1 μg/mL. Then 1 mL was added to each well, and the cells were incubated on the benchtop for 5 min, then washed twice with cold PBS, and immediately imaged. Fluorescence images were captured using a Cytation5 microplate reader equipped with fluorescent microscope (BioTek), with fluorescent filter cubes of emission (nm)/excitation (nm) = 469/525. Images were taken using a 4× objective.

Fluorescence Imaging of Cell uptake of DiI-Loaded PNPs. MCF-7 cells were seeded at a density of 1.0×10^5 cells per well in a 6-well plate (Costar) and allowed to adhere, as described in the previous section. Aqueous DiI-PNP formulations were mixed 1:5 with the cell media for a final PNP concentration of 0.05 mg/mL. After overnight incubation, cells were washed once with PBS, and the media was replaced with 1 mL of the media/PNP mixture. Cells were incubated for 2 h and then were washed twice with cold PBS. 4′,6-diamidino-2-phenylindole (DAPI, Life Technologies) was dissolved at a concentration of 1 μg/mL in DMSO and further diluted 10-fold in

PBS to afford a final concentration of 0.1 μg/mL. Then 1 mL was added to each well, and the cells were incubated on the benchtop for 5 min, then washed twice with cold PBS, and immediately imaged. Fluorescence images were captured using a Cytation5 microplate reader equipped with fluorescent microscope (BioTek), with fluorescent filter cubes of emission (nm)/excitation (nm) = 377/447 and 586/647. Images were taken using a 20× objective.

Flow Cytometry. Flow cytometry measurements were performed to quantify the cell uptake of the DiI-PNPs by MCF-7 cells. MCF-7 cells were seeded at a density of 5×10^5 cells per well in a 6-well plate (Costar) and allowed to adhere, as described in previous sections. Aqueous DiI-PNP formulations were mixed 1:5 with the cell media for a finial PNP concentration of 0.05 mg/mL. After overnight incubation, cells were washed once with PBS, and the media was replaced with 2 mL of the media/PNP mixture. Cells were incubated for 2 h, then washed twice with cold PBS, trypsinized, collected, and pelleted by centrifugation (5 min at 1,400 rpm). The cell pellet was then suspended in 200 μL PBS with 10% FBS. Cellular fluorescence was measured using a Beckman Coulter CytoFLEX and data was analyzed using CytExpert (Beckman Coulter). Mean fluorescence intensities of gated MCF-7 cells was recorded in the PE detection channel (585/42 filter). Reported values were determined from triplicate preparations of each DiI-PNP formulation, with each preparation being tested 3 times. Standard errors (σ) were calculated from the standard deviation (s) of triplicate values: $\sigma = \frac{s}{\sqrt{3}}$.

Statistics and Data Handling. For comparison of any two results in a data set, Excel built-in functions were used. The combined standard error SE_c was calculated from the square of the sum if the squares of the SEs from the individual data points:

$$SE_c = \sqrt{SE_1^2 + SE_2^2} \qquad (15)$$

Next, the combined degrees of freedom (DOF) were calculated on the basis of the number of values (N) in each data set:

$$DOF = [(N_1 - 1) + (N_2 - 1)] \qquad (16)$$

The difference between measured results (t) was expressed in terms of the difference between mean values, $\bar{x}$, over the combined standard error, SE_c:

$$t = \frac{|\overline{x_1} - \overline{x_2}|}{SE_c} \qquad (17)$$

Finally, a p-value was calculated for pairwise comparisons using the TDIST function:

$$p = \mathrm{TDIST}(t, \mathrm{DOF}, 2) \qquad (18)$$

where differences were assumed to be statistically significant when $p < 0.05$.

Supporting Information

Bright-field and fluorescence images for *EH* determination; workflows for *EH* and $RA_{compart}$ determination; TEM images of PAX-PNPs at different time points during PAX release experiments; $d_{h,eff}$ and $RA_{compart}$ values of PAX-PNPs at different time points during PAX release experiments; cell viability raw data for EC_{50} determinations

and associated controls; complete flow cytometry data and gating definitions; long-term stability test of PAX-PNPs; table of actual flow rates.

Corresponding Author

* E-mail: mmoffitt@uvic.ca.

Notes

The authors declare no competing financial interest.

Acknowledgement

We are grateful to the Natural Sciences and Engineering Research Council of Canada, NSERC, for financial support. We acknowledge Prof. Patrick Nahirney and Brent Gowen in the UVic EM lab (Department of Biology) for the continued use of their TEM. We also thank Rebecca Hof in the CAMTEC FBS facility for the training and assistance in cell-based assays and fluorescence measurements and Prof. Jeremy E. Wulff for extremely helpful discussions regarding the cell culture experiments.

References

1. Allen, C.; Maysinger, D.; Eisenberg, A., Nano-Engineering Block Copolymer Aggregates for Drug Delivery. *Colloids Surf., B* **1999**, *16*, 3-27.

2. Kataoka, K.; Harada, A.; Nagasaki, Y., Block Copolymer Micelles for Drug Delivery: Design, Characterization and Biological Significance. *Adv. Drug Delivery Rev.* **2001**, *47*, 113-131.

3. Rösler, A.; Vandermeulen, G. W. M.; Klok, H.-A., Advanced Drug Delivery Devices *via* Self-Assembly of Amphiphilic Block Copolymers. *Adv. Drug Delivery Rev.* **2001**, *53*, 95-108.

4. Davis, M. E.; Chen, Z.; Shin, D. M., Nanoparticle Therapeutics: An Emerging Treatment Modality for Cancer. *Nat. Rev. Drug Discov.* **2008**, *7*, 771-782.

5. Tyrrell, Z. L.; Shen, Y.; Radosz, M., Fabrication of Micellar Nanoparticles for Drug Delivery through the Self-Assembly of Block Copolymers. *Prog. Polym. Sci.* **2010**, *35*, 1128-1143.

6. Gong, J.; Chen, M.; Zheng, Y.; Wang, S.; Wang, Y., Polymeric Micelles Drug Delivery System in Oncology. *J. Controlled Release* **2012**, *159*, 312-323.

7. Sun, T.; Zhang, Y. S.; Pang, B.; Hyun, D. C.; Yang, M.; Xia, Y., Engineered Nanoparticles for Drug Delivery in Cancer Therapy. *Angew. Chem. Int. Ed.* **2014**, *53*, 12320-12364.

8. Björnmalm, M.; Thurecht, K. J.; Michael, M.; Scott, A. M.; Caruso, F., Bridging Bio–Nano Science and Cancer Nanomedicine. *ACS Nano* **2017**, *11*, 9594-9613.

9. Kakkar, A.; Traverso, G.; Farokhzad, O. C.; Weissleder, R.; Langer, R., Evolution of Macromolecular Complexity in Drug Delivery Systems. *Nat. Rev. Chem.* **2017**, *1*, 0063.

10. Cao, J.; Huang, D.; Peppas, N. A., Advanced Engineered Nanoparticulate Platforms to Address Key Biological Barriers for Delivering Chemotherapeutic Agents to Target Sites. *Adv. Drug Delivery Rev.* **2020**. DOI: 10.1016/j.addr.2020.06.030

11. Schudel, A.; Chapman, A. P.; Yau, M.-K.; Higginson, C. J.; Francis, D. M.;

Manspeaker, M. P.; Avecilla, A. R. C.; Rohner, N. A.; Finn, M. G.; Thomas, S. N., Programmable Multistage Drug Delivery to Lymph Nodes. *Nat. Nanotechnol.* **2020**, *15*, 491-499.

12. Zhang, P.; Gao, D.; An, K.; Shen, Q.; Wang, C.; Zhang, Y.; Pan, X.; Chen, X.; Lyv, Y.; Cui, C.; Liang, T.; Duan, X.; Liu, J.; Yang, T.; Hu, X.; Zhu, J.-J.; Xu, F.; Tan, W. A Programmable Polymer Library that Enables the Construction of Stimuli-Responsive Nanocarriers Containing Logic Gates. *Nat. Chem.* **2020**, *12*, 381-390.

13. Alexis, F.; Pridgen, E.; Molnar, L. K.; Farokhzad, O. C., Factors Affecting the Clearance and Biodistribution of Polymeric Nanoparticles. *Mol. Pharmaceutics* **2008**, *5*, 505-515.

14. Elsabahy, M.; Wooley, K. L., Design of Polymeric Nanoparticles for Biomedical Delivery Applications. *Chem. Soc. Rev.* **2012**, *41*, 2545-2561.

15. Maeda, H.; Wu, J.; Sawa, T.; Matsumura, Y.; Hori, K., Tumor Vascular Permeability and the EPR Effect in Macromolecular Therapeutics: A Review. *J. Controlled Release* **2000**, *65*, 271-284.

16. Maeda, H.; Nakamura, H.; Fang, J., The EPR Effect for Macromolecular Drug Delivery to Solid Tumors: Improvement of Tumor Uptake, Lowering of Systemic Toxicity, and Distinct Tumor Imaging in Vivo. *Adv. Drug Delivery Rev.* **2013**, *65*, 71-79.

17. Perry, J. L.; Reuter, K. G.; Luft, J. C.; Pecot, C. V.; Zamboni, W.; DeSimone, J. M., Mediating Passive Tumor Accumulation through Particle Size, Tumor Type, and

Location. *Nano Lett.* **2017**, *17*, 2879-2886.

18. Geng, Y.; Dalhaimer, P.; Cai, S.; Tsai, R.; Tewari, M.; Minko, T.; Discher, D. E., Shape Effects of Filaments Versus Spherical Particles in Flow and Drug Delivery. *Nat. Nanotechnol.* **2007**, *2*, 249-255.

19. Gaumet, M.; Vargas, A.; Gurny, R.; Delie, F., Nanoparticles for Drug Delivery: The Need for Precision in Reporting Particle Size Parameters. *Euro. J. Pharm. Biopharm.* **2008**, *69*, 1-9.

20. Fairley, N.; Hoang, B.; Allen, C., Morphological Control of Poly(Ethylene Glycol)-Block-Poly(ε-Caprolactone) Copolymer Aggregates in Aqueous Solution. *Biomacromolecules* **2008**, *9*, 2283-2291.

21. Venkataraman, S.; Hedrick, J. L.; Ong, Z. Y.; Yang, C.; Ee, P. L. R.; Hammond, P. T.; Yang, Y. Y., The Effects of Polymeric Nanostructure Shape on Drug Delivery. *Adv. Drug Delivery Rev.* **2011**, *63*, 1228-1246.

22. Russo, A.; DeGraff, W.; Friedman, N.; Mitchell, J. B., Selective Modulation of Glutathione Levels in Human Normal Versus Tumor Cells and Subsequent Differential Response to Chemotherapy Drugs. *Cancer Res.* **1986**, *46*, 2845.

23. Jiang, X. Q.; Yu, Y.; Chen, J. W.; Zhao, M. K.; Chen, H.; Song, X. Z.; Matzuk, A. J.; Carroll, S. L.; Tan, X.; Sizovs, A.; Cheng, N. H.; Wang, M. C.; Wang, J., Quantitative Imaging of Glutathione in Live Cells Using a Reversible Reaction-Based Ratiometric Fluorescent Probe. *ACS Chem. Biol.* **2015**, *10*, 864-874.

24. Saito, G.; Swanson, J. A.; Lee, K.-D., Drug Delivery Strategy Utilizing Conjugation

via Reversible Disulfide Linkages: Role and Site of Cellular Reducing Activities. *Adv. Drug Delivery Rev.* **2003**, *55*, 199-215.

25. Klaikherd, A.; Nagamani, C.; Thayumanavan, S., Multi-Stimuli Sensitive Amphiphilic Block Copolymer Assemblies. *J. Am. Chem. Soc.* **2009**, *131*, 4830-4838.

26. Tang, L.-Y.; Wang, Y.-C.; Li, Y.; Du, J.-Z.; Wang, J., Shell-Detachable Micelles Based on Disulfide-Linked Block Copolymer as Potential Carrier for Intracellular Drug Delivery. *Bioconjugate Chem.* **2009**, *20*, 1095-1099.

27. Khorsand, B.; Lapointe, G.; Brett, C.; Oh, J. K., Intracellular Drug Delivery Nanocarriers of Glutathione-Responsive Degradable Block Copolymers Having Pendant Disulfide Linkages. *Biomacromolecules* **2013**, *14*, 2103-2111.

28. Cunningham, A.; Oh, J. K., New Design of Thiol-Responsive Degradable Polylactide-Based Block Copolymer Micelles. *Macromol. Rapid Commun.* **2013**, *34*, 163-168.

29. Oh, J. K., Disassembly and Tumor-Targeting Drug Delivery of Reduction-Responsive Degradable Block Copolymer Nanoassemblies. *Polym. Chem.* **2019**, *10*, 1554-1568.

30. Biswas, D.; An, S. Y.; Li, Y.; Wang, X.; Oh, J. K., Intracellular Delivery of Colloidally Stable Core-Cross-Linked Triblock Copolymer Micelles with Glutathione-Responsive Enhanced Drug Release for Cancer Therapy. *Mol. Pharmaceutics* **2017**, *14*, 2518-2528.

31. Chan, N.; Khorsand, B.; Aleksanian, S.; Oh, J. K., A Dual Location Stimuli-

Responsive Degradation Strategy of Block Copolymer Nanocarriers for Accelerated Release. *Chem. Commun.* **2013**, *49*, 7534-7536.

32. Chen, W.; Yang, H.; Wang, R.; Cheng, R.; Meng, F.; Wei, W.; Zhong, Z., Versatile Synthesis of Functional Biodegradable Polymers by Combining Ring-Opening Polymerization and Postpolymerization Modification *via* Michael-Type Addition Reaction. *Macromolecules* **2010**, *43*, 201-207.

33. Liu, J.; Huang, W.; Pang, Y.; Zhu, X.; Zhou, Y.; Yan, D., Hyperbranched Polyphosphates for Drug Delivery Application: Design, Synthesis, and In Vitro Evaluation. *Biomacromolecules* **2010**, *11*, 1564-1570.

34. Zhang, Q.; Ko, N. R.; Oh, J. K., Recent Advances in Stimuli-Responsive Degradable Block Copolymer Micelles: Synthesis and Controlled Drug Delivery Applications. *Chem. Commun.* **2012**, *48*, 7542-7552.

35. Zhang, Q.; Ko, N. R. ; Oh, J. K., Modulated Morphologies and Tunable Thiol-Responsive Shedding of Aqueous Block Copolymer Aggregates. *RSC Adv.* **2012**, *2*, 8079-8086.

36. Capretto, L.; Carugo, D.; Mazzitelli, S.; Nastruzzi, C.; Zhang, X., Microfluidic and Lab-on-a-Chip Preparation Routes for Organic Nanoparticles and Vesicular Systems for Nanomedicine Applications. *Adv. Drug Delivery Rev.* **2013**, *65*, 1496-1532.

37. Karnik, R.; Gu, F.; Basto, P.; Cannizzaro, C.; Dean, L.; Kyei-Manu, W.; Langer, R.; Farokhzad, O. C., Microfluidic Platform for Controlled Synthesis of Polymeric Nanoparticles. *Nano Lett.* **2008**, *8*, 2906-2912.

38. Xu, Q.; Hashimoto, M.; Dang, T. T.; Hoare, T.; Kohane, D. S.; Whitesides, G. M.; Langer, R.; Anderson, D. G., Preparation of Monodisperse Biodegradable Polymer Microparticles Using a Microfluidic Flow-Focusing Device for Controlled Drug Delivery. *Small* **2009**, *5*, 1575-1581.

39. Zhang, Y.; Chan, H. F.; Leong, K. W., Advanced Materials and Processing for Drug Delivery: The Past and the Future. *Adv. Drug Delivery Rev.* **2013**, *65*, 104-120.

40. Schabas, G.; Wang, C.-W.; Oskooei, A.; Yusuf, H.; Moffitt, M. G.; Sinton, D., Formation and Shear-Induced Processing of Quantum Dot Colloidal Assemblies in a Multiphase Microfluidic Chip. *Langmuir* **2008**, *24*, 10596-10603.

41. Schabas, G.; Yusuf, H.; Moffitt, M. G.; Sinton, D., Controlled Self-Assembly of Quantum Dots and Block Copolymers in a Microfluidic Device. *Langmuir* **2008**, *24*, 637-643.

42. Wang, C.-W.; Oskooei, A.; Sinton, D.; Moffitt, M. G., Controlled Self-Assembly of Quantum Dot−Block Copolymer Colloids in Multiphase Microfluidic Reactors. *Langmuir* **2010**, *26*, 716-723.

43. Wang, C.-W.; Sinton, D.; Moffitt, M. G., Flow-Directed Block Copolymer Micelle Morphologies *via* Microfluidic Self-Assembly. *J. Am. Chem. Soc.* **2011**, *133*, 18853-18864.

44. Wang, C.-W.; Bains, A.; Sinton, D.; Moffitt, M. G., Flow-Directed Assembly of Block Copolymer Vesicles in the Lab-on-a-Chip. *Langmuir* **2012**, *28*, 15756-15761.

45. Wang, C.-W.; Bains, A.; Sinton, D.; Moffitt, M. G., Flow-Directed Loading of Block

Copolymer Micelles with Hydrophobic Probes in a Gas–Liquid Microreactor. *Langmuir* **2013**, *29*, 8385-8394.

46. Wang, C.-W.; Sinton, D.; Moffitt, M. G., Morphological Control *via* Chemical and Shear Forces in Block Copolymer Self-Assembly in the Lab-on-Chip. *ACS Nano* **2013**, *7*, 1424-1436.

47. Bains, A.; Cao, Y.; Moffitt, M. G., Multiscale Control of Hierarchical Structure in Crystalline Block Copolymer Nanoparticles Using Microfluidics. *Macromol. Rapid Commun.* **2015**, *36*, 2000-2005.

48. Xu, Z.; Yan, B.; Riordon, J.; Zhao, Y.; Sinton, D.; Moffitt, M. G., Microfluidic Synthesis of Photoresponsive Spool-Like Block Copolymer Nanoparticles: Flow-Directed Formation and Light-Triggered Dissociation. *Chem. Mater.* **2015**, *27*, 8094-8104.

49. Bains, A.; Wulff, J. E.; Moffitt, M. G., Microfluidic Synthesis of Dye-Loaded Polycaprolactone-Block-Poly(Ethylene Oxide) Nanoparticles: Insights into Flow-Directed Loading and In Vitro Release for Drug Delivery. *J. Colloid Interface Sci.* **2016**, *475*, 136-148.

50. Xu, Z.; Lu, C.; Riordon, J.; Sinton, D.; Moffitt, M. G., Microfluidic Manufacturing of Polymeric Nanoparticles: Comparing Flow Control of Multiscale Structure in Single-Phase Staggered Herringbone and Two-Phase Reactors. *Langmuir* **2016**, *32*, 12781-12789.

51. Bains, A.; Cao, Y.; Kly, S.; Wulff, J. E.; Moffitt, M. G., Controlling Structure and

Function of Polymeric Drug Delivery Nanoparticles Using Microfluidics. *Mol. Pharmaceutics* **2017**, *14*, 2595-2606.

52. Xu, Z.; Lu, C.; Lindenberger, C.; Cao, Y.; Wulff, J. E.; Moffitt, M. G., Synthesis, Self-Assembly, and Drug Delivery Characteristics of Poly(Methyl Caprolactone-Co-Caprolactone)-b-Poly(Ethylene Oxide) Copolymers with Variable Compositions of Hydrophobic Blocks: Combining Chemistry and Microfluidic Processing for Polymeric Nanomedicines. *ACS Omega* **2017**, *2*, 5289-5303.

53. Chen, R.; Wulff, J. E.; Moffitt, M. G., Microfluidic Processing Approach to Controlling Drug Delivery Properties of Curcumin-Loaded Block Copolymer Nanoparticles. *Mol. Pharmaceutics* **2018**, *15*, 4517-4528.

54. Cao, Y.; Silverman, L.; Lu, C.; Hof, R.; Wulff, J. E.; Moffitt, M. G., Microfluidic Manufacturing of SN-38-Loaded Polymer Nanoparticles with Shear Processing Control of Drug Delivery Properties. *Mol. Pharmaceutics* **2019**, *16*, 96-107.

55. Huang, Y.; Moini Jazani, A.; Howell, E. P.; Oh, J. K.; Moffitt, M. G., Controlled Microfluidic Synthesis of Biological Stimuli-Responsive Polymer Nanoparticles. *ACS Appl. Mater. Interfaces* **2020**, *12*, 177-190.

56. Hong, R.; Han, G.; Fernández, J. M.; Kim, B.-J.; Forbes, N. S.; Rotello, V. M., Glutathione-Mediated Delivery and Release Using Monolayer Protected Nanoparticle Carriers. *J. Am. Chem. Soc.* **2006**, *128*, 1078-1079.

For Table of Contents Use Only

Microfluidic Shear Processing Control of Biological Reduction-Responsive Polymer Nanoparticles for Drug Delivery

Yuhang Huang, Arman Moini Jazani, Elliot P. Howell, Lisa A. Reynolds, Jung Kwon Oh, and Matthew G. Moffitt